CellPress

Neuron
Article

A TRPV Channel in *Drosophila* Motor Neurons Regulates Presynaptic Resting Ca^{2+} Levels, Synapse Growth, and Synaptic Transmission

Ching-On Wong,[1] Kuchuan Chen,[2] Yong Qi Lin,[3,4,10] Yufang Chao,[1] Lita Duraine,[3,4] Zhongmin Lu,[5] Wan Hee Yoon,[3,4] Jeremy M. Sullivan,[6] Geoffrey T. Broadhead,[1] Charlotte J. Sumner,[6,7] Thomas E. Lloyd,[6,7] Gregory T. Macleod,[8,11] Hugo J. Bellen,[2,3,4] and Kartik Venkatachalam[1,2,9,*]

[1]Department of Integrative Biology and Pharmacology, University of Texas School of Medicine, 6431 Fannin Street, Houston, TX 77030, USA
[2]Graduate Program in Developmental Biology, Baylor College of Medicine, 1250 Moursund Street, Suite N1125.14, Mailstop NR-1125, Houston, TX 77030, USA
[3]Howard Hughes Medical Institute
[4]Departments of Molecular and Human Genetics and Neuroscience, Baylor College of Medicine, 1250 Moursund Street, Suite N1125.14, Mailstop NR-1125, Houston, TX 77030, USA
[5]Integrative Biology and Neuroscience program, Florida Atlantic University and Max Planck Florida Institute, 5353 Parkside Drive, Jupiter, FL 33458, USA
[6]Department of Neurology
[7]Department of Neuroscience
Johns Hopkins University School of Medicine, 855 North Wolfe Street, Baltimore, MD 21231, USA
[8]Department of Physiology, University of Texas Health Science Center, 7703 Floyd Curl Drive, San Antonio, TX 78229, USA
[9]Graduate Programs in Cell and Regulatory Biology (CRB) and Neuroscience, Graduate School of Biomedical Sciences, University of Texas School of Medicine, Houston, TX 77030
[10]Present address: Functional Genomics Group, Neuroscience Program, Garvan Institute of Medical Research, 384 Victoria Street, Darlinghurst NSW 2010, Australia
[11]Present address: Department of Biological Sciences, Florida Atlantic University, 5353 Parkside Drive, Jupiter, FL 33458, USA
*Correspondence: kartik.venkatachalam@uth.tmc.edu
http://dx.doi.org/10.1016/j.neuron.2014.09.030

SUMMARY

Presynaptic resting Ca^{2+} influences synaptic vesicle (SV) release probability. Here, we report that a TRPV channel, Inactive (Iav), maintains presynaptic resting [Ca^{2+}] by promoting Ca^{2+} release from the endoplasmic reticulum in *Drosophila* motor neurons, and is required for both synapse development and neurotransmission. We find that Iav activates the Ca^{2+}/calmodulin-dependent protein phosphatase calcineurin, which is essential for presynaptic microtubule stabilization at the neuromuscular junction. Thus, loss of Iav induces destabilization of presynaptic microtubules, resulting in diminished synaptic growth. Interestingly, expression of human TRPV1 in Iav-deficient motor neurons rescues these defects. We also show that the absence of Iav causes lower SV release probability and diminished synaptic transmission, whereas Iav overexpression elevates these synaptic parameters. Together, our findings indicate that Iav acts as a key regulator of synaptic development and function by influencing presynaptic resting [Ca^{2+}].

INTRODUCTION

At any time, the Ca^{2+} concentration ([Ca^{2+}]) within presynaptic terminals is a function of the complex interplay between events driving Ca^{2+} elevation and Ca^{2+} sequestration. Presynaptic Ca^{2+} elevation, which may occur due to depolarization-induced opening of voltage-gated Ca^{2+} channels (VGCCs), triggers SV exocytosis (Catterall, 2000). While VGCCs are closed, the resting [Ca^{2+}] is insufficient to trigger SV release but influences SV release probability and sculpts the spatiotemporal dynamics of synaptic transmission (Awatramani et al., 2005; Zucker and Regehr, 2002). However, whether resting [Ca^{2+}] is involved in other aspects of presynaptic function and whether specific non-excitatory channels set the resting [Ca^{2+}] remain unknown.

We sought to evaluate the synaptic function of Ca^{2+} channels belonging to the transient receptor potential (TRP) superfamily, which are voltage-independent channels that regulate diverse neuronal pathways (Venkatachalam and Montell, 2007). However, the biggest hurdle to evaluating the role of TRP channels in synapse development and function is the extent of functional redundancy between the different vertebrate TRP genes (Venkatachalam and Montell, 2007). This problem can be overcome by using *Drosophila*, because flies express only 13 TRP genes compared to the 27 in vertebrates (Venkatachalam and Montell, 2007). Moreover, loss-of-function mutations in all 13 *Drosophila* TRP genes are available (Fowler and Montell, 2013). We found that loss-of-function mutations in a *Drosophila* TRPV channel gene, *inactive* (*iav*) (Gong et al., 2004), result in decreased synaptic growth and diminished neurotransmission. Our results indicate that Iav functions in motor neurons (MNs) to regulate ER Ca^{2+} release and is required for maintaining presynaptic resting [Ca^{2+}], which is essential for microtubule stability, synaptic growth, and SV release probability.

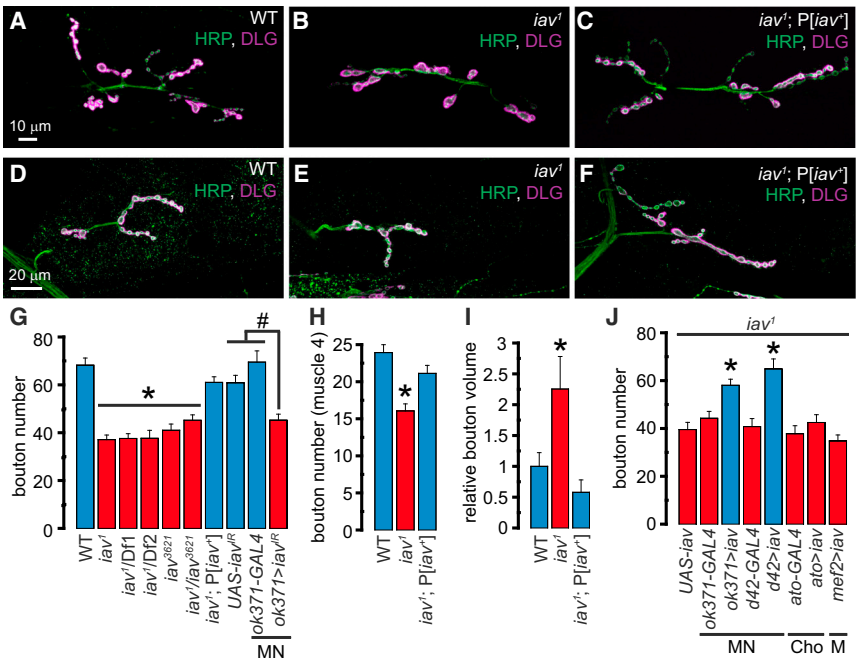

Figure 1. Alterations in Synaptic Growth and Morphology in *iav*^{1}

(A–C) Confocal images of NMJs on muscles 6/7 from larvae of the indicated genotypes stained with antibodies against the presynaptic marker, HRP (green), and the postsynaptic marker, DLG (magenta). Scale bar shown in (A) also applies to (B) and (C).

(D–F) Confocal images of NMJs on muscle 4 from larvae of the indicated genotypes stained with antibodies against HRP (green) and DLG (magenta). Scale bar shown in (D) also applies to (E) and (F).

(G) Quantification of the number of boutons at NMJs on muscles 6/7 in larvae of the indicated genotypes. *p < 0.0001, one-way ANOVA (comparing all the *iav*^{1} alleles with WT and *iav*^{1} ;P[*iav*$^{+}$]; #p = 2.5 × 10^{-5}, one-way ANOVA; comparing *ok371* > *iav*^{IR} with *GAL4* and *UAS* controls); n = 8–30 NMJs per genotype.

(H) Quantification of the number of boutons at NMJs on muscle 4 in larvae of the indicated genotypes. *p = 6.3 × 10^{-6}, one-way ANOVA (comparing all the data sets shown), n = 8–14 NMJs per genotype.

(I) Quantification of the volume/bouton in larvae of the indicated genotypes. *p = 0.007, one-way ANOVA (comparing all the data sets shown), n ≥ 7 NMJs per genotype.

(J) Quantification of the bouton number in larvae of the indicated genotypes. *p < 10^{-6}, one-way ANOVA (comparing the data sets shown in the blue bars with those in the red bars), n = 11–20 NMJs per genotype.

All values represent mean ± SEM. Please consult the Supplemental Information for values. Abbreviations: MN, motor neuron; Cho, chordotonal organ; M, muscle.

RESULTS

Inactive Is Required for Synapse Growth and Morphology

We determined the number of synaptic boutons at the *Drosophila* third-instar larval NMJs in wild-type and loss-of-function alleles of the TRP channel genes indicated in Table S1 (available online) using antibodies against horseradish peroxidase (HRP, which detects a carbohydrate moiety present on numerous neuronal glycoproteins; Snow et al., 1987) and Discs large (DLG, *Drosophila* ortholog of PSD-95; Cho et al., 1992). Only the larvae lacking *iav* (Gong et al., 2004) exhibit fewer synaptic boutons (muscles 6/7), which are 2-fold larger than control boutons (Table S1; Figures 1A, 1B, 1G, and 1I). The *iav* mutants (*iav*^{1}) also exhibit diminished bouton numbers at the NMJs on muscle 4 (Figures 1D, 1E, and 1H). The alterations in bouton numbers and size are rescued by a genomic wild-type *iav* transgene (P[*iav*$^{+}$]) (Figures 1C, 1F, and 1G–1I). The *iav*^{1}/Df1, *iav*^{1}/Df2, *iav*^{3621}, and *iav*^{1} /*iav*^{3621} larvae (Gong et al., 2004) also show similar alterations in the bouton number and morphology (Figure 1G).

Iav Functions in Motor Neurons to Regulate NMJ Synapse Growth

To assess whether synaptic growth defects in *iav*^{1} are due to a requirement for Iav in MNs, we first expressed an RNAi against *iav* (*UAS-iav*^{IR}) in MNs using the *VGLUT*^{ok371}*-GAL4* (*ok371-GAL4*) driver. Expression of *iav*^{IR} in wild-type MNs induces a significant decrease in NMJ bouton number—a phenotype not observed in the *UAS/GAL4* controls (Figure 1G). Furthermore, expression of *UAS-iav* in the *iav*^{1} MNs using two separate drivers, *ok371-GAL4* and *d42-GAL4*, rescues the synaptic growth defects (Figure 1J).

Iav is expressed in chordotonal neurons, where it is required for hearing (Gong et al., 2004). However, we found that expression of *UAS-iav* in the *iav*^{1} chordotonal organs using *ato-Gal4* (*iav*^{1}; *ato > iav)* does not suppress the NMJ phenotype (Figure 1J). Expression of *iav* in mutant muscles (*iav*^{1}; *mef2 > iav*) also does not restore the bouton number in *iav*^{1} (Figure 1J). These data indicate that Iav functions cell-autonomously in MNs to drive synaptic growth.

Human TRPV1, but neither Human TRPV4 nor *Drosophila* Nanchung, Rescues the *iav*^{1} Synaptic Growth Phenotype

Within the hTRPV channel subfamily (hTRPV1-6, 25%–27% identity and 39%–46% similarity with Iav), hTRPV1 and hTRPV4 are the most extensively studied channels (Caterina et al., 1999, 2000; Güler et al., 2002; Watanabe et al., 2002), whose activity can be manipulated by a host of pharmacological agents (Watanabe et al., 2002; Xia et al., 2011a, 2011b). Here, we asked whether expression of either hTRPV1 of hTRPV4 in *iav*^{1} MNs would suppress the synaptic growth defects (see Figure S1 for a comparison of the amino acid sequences of Iav, hTRPV1, and hTRPV4). Remarkably, expression of hTRPV1 in the *iav*^{1} MNs (*iav*^{1}*; ok371 > hTRPV1*) suppresses the diminished synaptic growth (Figures 2A, 2B, and 2J). However, expression of hTRPV1 in wild-type MNs (*ok371>hTRPV1*) does not promote the formation of additional boutons (Figures 2C and 2J). We also pharmacologically inhibited the hTRPV1 channels expressed in the *iav*^{1} MNs by feeding the *iav*^{1}*; ok371 > hTRPV1* larvae the TRPV1

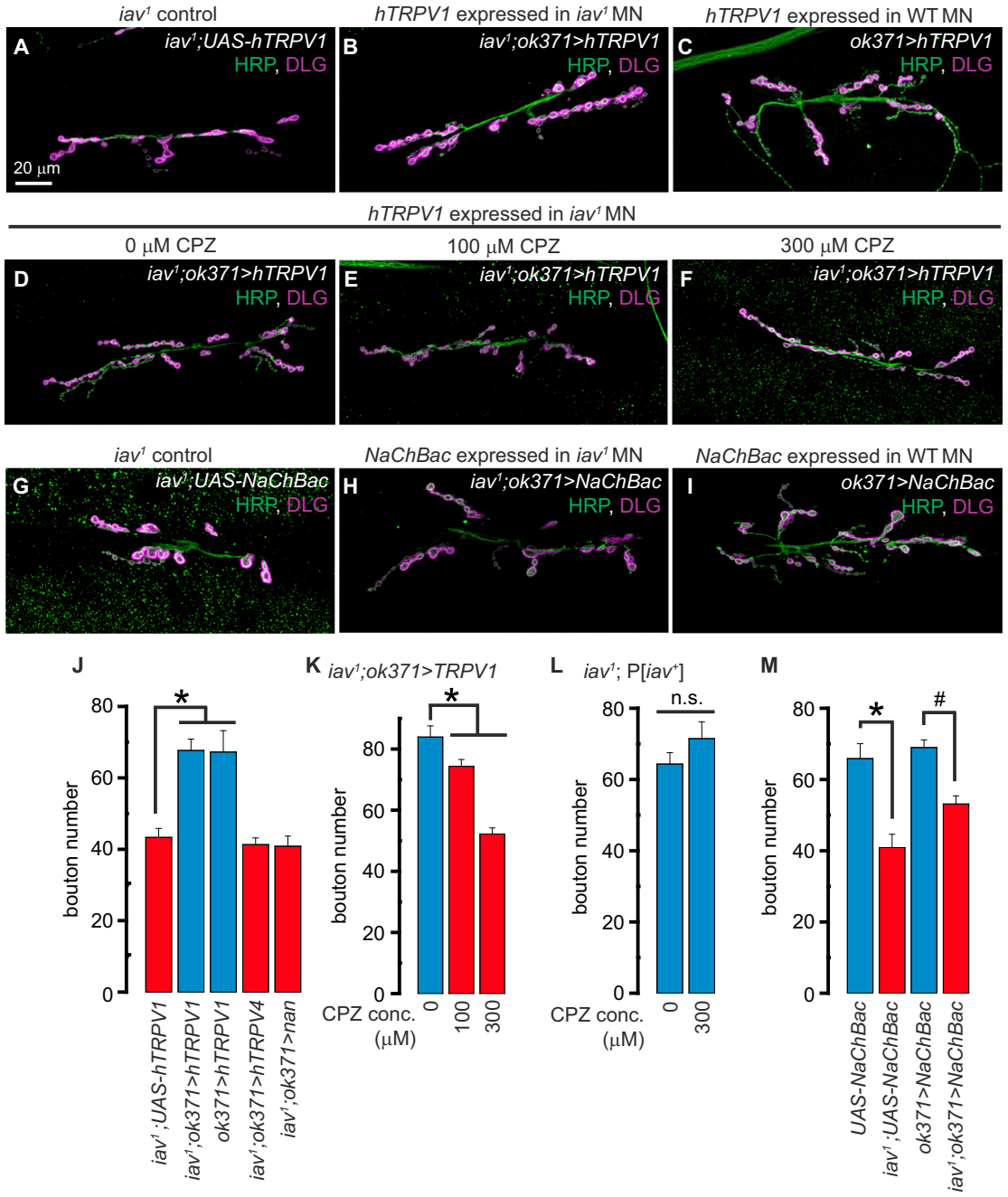

Figure 2. Suppression of *iav*^{1} Synaptic Growth Defects by Presynaptic Expression of Human TRPV1, but Not Human TRPV4

(A–C) Confocal images of larval NMJs from larvae of the indicated genotypes stained with antibodies against HRP (green) and DLG (magenta).

(D–F) Confocal images of larval NMJs from larvae of the indicated genotypes that were fed the indicated concentrations of capsazepine (CPZ) stained with antibodies against HRP (green) and DLG (magenta).

(G–I) Confocal images of NMJs from larvae of the indicated genotypes stained with antibodies against HRP (green) and DLG (magenta).

Scale bar shown in (A) also applies to (B)–(I).

(J) Quantification of the NMJ bouton number in larvae of the indicated genotypes. *p = 5.2 × 10^{-4}, one-way ANOVA, n = 9–12 NMJs per genotype.

(K and L) Quantification of the NMJ bouton numbers in larvae of the indicated genotypes that were fed the indicated concentrations of CPZ. The overall increased baseline of the bouton number in all the genotypes here was a result of raising the flies on instant food. In (K), *p = 10^{-9}, one-way ANOVA, n = 14–28 NMJs per genotype. In (L), n.s. represents "not significant," p = 0.22, unpaired Student's t test, n = 15 NMJs per genotype.

(M) Quantification of the NMJ bouton number in larvae of the indicated genotypes. *p = 4.4 × 10^{-4}, unpaired Student's t test, n = 8–9 NMJs per genotype; #p = 1.3 × 10^{-5}, unpaired Student's t test, n = 18–24 NMJs per genotype.

All values represent mean ± SEM. Abbreviations: WT, wild-type; MN, motor neuron; n.s., not significant.

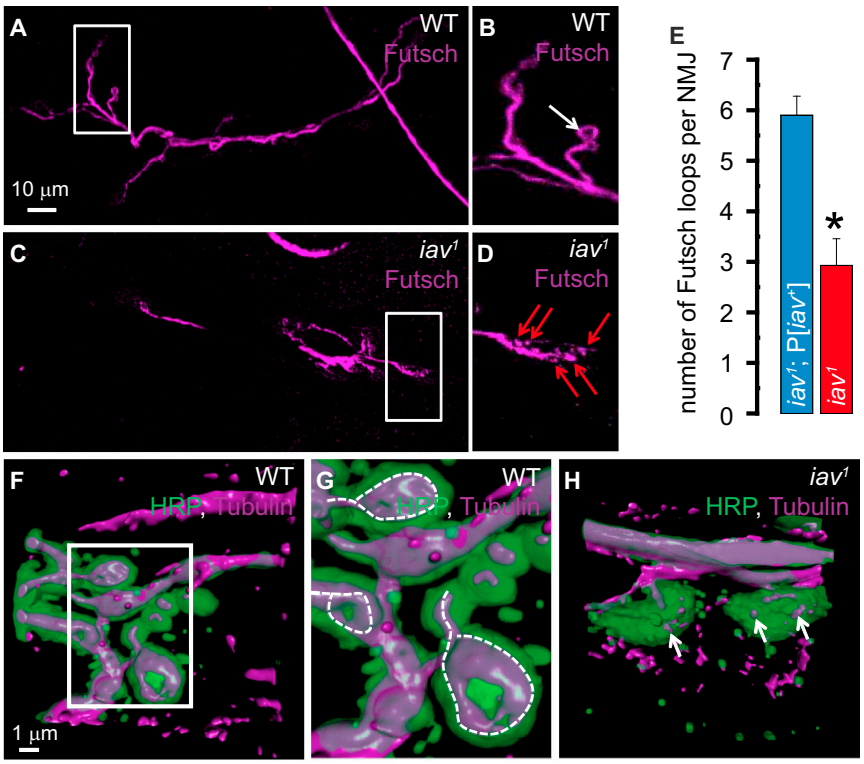

Figure 3. Disruption of the Presynaptic Microtubule Cytoskeleton in *iav*^{1}

(A) Confocal image of an NMJ from wild-type (WT) larvae stained with antibodies against Futsch (magenta).

(B) Magnification of the boxed region in (A). White arrow points to a synaptic Futsch loop.

(C) Same as (A), but in *iav*^{1} larvae. Scale bar shown in (A) also applies to (C).

(D) Same as (B), but in *iav*^{1} larvae. Red arrows point to synaptic Futsch punctae.

(E) Quantification of the number of Futsch loops per NMJ in the indicated genotypes. *p = 3.6 × 10^{-4}, Student's t test, n = 10–14 NMJs per genotype.

(F) 3D reconstruction of a wild-type (WT) synaptic bouton stained with antibodies against HRP (green) and tubulin (magenta).

(G) Magnification of the boxed region in (F). Dashed lines represent synaptic microtubule loops.

(H) Same as (F), but in *iav*^{1} larvae. Arrows point to fragmented microtubules. Scale bar shown in (F) also applies to (H).

(I) Schematic depicting the role of Futsch phosphorylation status on the regulation of presynaptic microtubule stability.

All values represent mean ± SEM. Abbreviations: MAP-1b, microtubule associated protein-1b; P, phosphorylation.

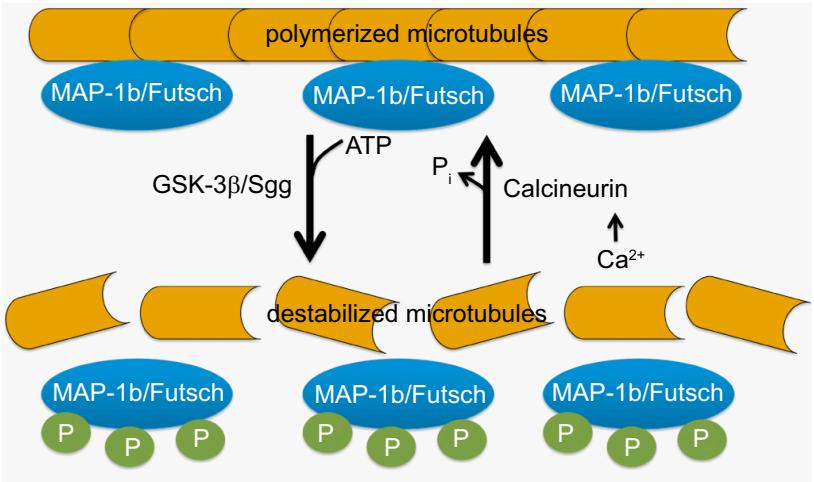

antagonist, capsazepine (CPZ) (Zygmunt et al., 1999). CPZ reverses the hTRPV1-mediated suppression of the *iav*^{1} synaptic growth phenotype in a dose-dependent manner (Figures 2D–2F and 2K), whereas even 300 μM of CPZ does not decrease synaptic growth in control *iav*^{1}; P[*iav*$^{+}$] neurons that lack hTRPV1 (Figure 2L). In contrast, expression of neither hTRPV4 nor *Drosophila* Nanchung (Nan, the second TRPV gene in *Drosophila*; Kim et al., 2003) in the *iav*^{1} MNs suppresses the synaptic growth defects (Figure 2J).

To test whether elevating MN neuronal activity is sufficient to suppress the *iav*^{1} synaptic growth phenotype, we expressed a constitutively active bacterial Na^{+} channel, NaChBac (Kuzmenkin et al., 2004; Luan et al., 2006), in the *iav*^{1} MNs. NaChBac depolarizes the host neurons and decreases their threshold for firing action potentials (Kuzmenkin et al., 2004). In contrast to the rescue we observed with expression of hTRPV1, the *iav*^{1} NMJ synaptic growth defects persist following the expression of NaChBac (Figures 2G–2I, and 2M). These data indicate that the synaptic growth phenotype at the *iav*^{1} NMJs depends on the selective loss of TRPV channel activity rather than diminished MN excitability.

Decreased Microtubule Stability in *iav*^{1} Motor Neurons

The decrease in synaptic bouton number with a concomitant increase in bouton volume in *iav*^{1} is reminiscent of the phenotype observed in larvae lacking genes such as *wingless* (Miech et al., 2008; Packard et al., 2002), *vapb* (encoding Vesicle Associated Membrane Protein-B) (Nishimura et al., 2004; Pennetta et al., 2002), *futsch* (the fly ortholog of the gene encoding mammalian microtubule associated protein-1b, MAP-1b) (Roos et al., 2000; Zhang et al., 2001), and *pp2A-B′* (a subunit of the PP2A protein phosphatase) (Viquez et al., 2006). Because diminished stability of presynaptic microtubules underlies the synaptic defects in these mutants, we assessed the structure of the presynaptic microtubules in *iav*^{1}. First, we found that the number of the characteristic Futsch loops is reduced by ~50% within *iav*^{1} synapses compared to controls (Figures 3A–3E). Moreover, in

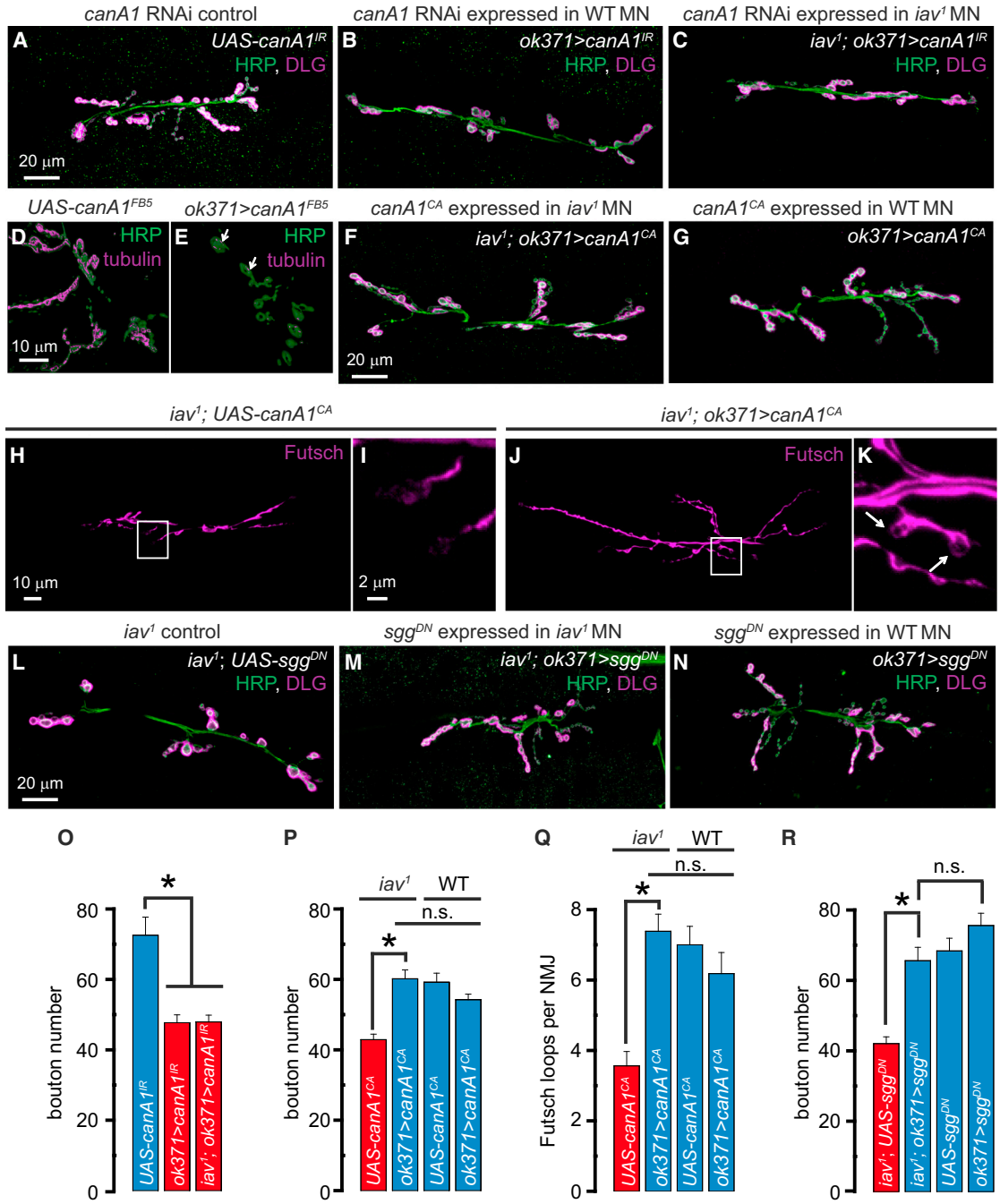

Figure 4. Role of Calcineurin in the *iav*^{1} Synaptic Growth Phenotype

(A–C) Confocal images of NMJs from larvae of the indicated genotypes stained with antibodies against HRP (green) and DLG (magenta). Scale bar shown in (A) also applies to (B) and (C).

(D and E) 3D reconstruction of synaptic boutons from larvae of the indicated genotypes stained with antibodies against HRP (green) and tubulin (magenta). Please note that only the microtubules within the NMJ boutons are shown by applying an "HRP mask" (see Experimental Procedures). Scale bar shown in (D) also applies to (E).

(F and G) Confocal images of NMJs from larvae of the indicated genotypes stained with antibodies against HRP (green) and DLG (magenta). Scale bar shown in (F) also applies to (G).

(H and J) Confocal images of NMJs from larvae of the indicated genotypes stained with antibodies against Futsch (magenta). Scale bar shown in (H) also applies to (J).

(I and K) Magnification of the boxed regions in (H) and (J), respectively. Scale bar shown in (I) also applies to (K). Arrows in (K) point to Futsch loops.

(legend continued on next page)

contrast to the Futsch loops within control boutons (Figure 3B, arrow points to a Futsch loop), Futsch appears punctate within some *iav*^{1} boutons (Figure 3D, red arrows point to Futsch punctae). Next, 3D reconstructions of synaptic boutons stained with an anti-tubulin antibody revealed the characteristic loop-like structures that microtubules form within wild-type boutons (Figures 3F and dashed lines in Figure 3G). However, microtubules appear fragmented in *iav*^{1} boutons (Figure 3H, arrows) further indicating that the presynaptic microtubules exhibit diminished stability at the *iav*^{1} NMJs.

Diminished Calcineurin Activity Underlies the Synaptic Growth Defects in *iav*^{1}

The stability of presynaptic microtubules depends on the level and/or phosphorylation status of Futsch (Franco et al., 2004; Miech et al., 2008; Packard et al., 2002; Roos et al., 2000) (Figure 3I). Thus, *futsch*-deficient larvae exhibit diminished bouton numbers and increased bouton size (Roos et al., 2000)—a phenotype similar to that observed in *iav*^{1}. The *Drosophila* homolog of glycogen synthase kinase-3β (GSK-3β), Shaggy (Sgg), phosphorylates Futsch, causing the latter to dissociate from microtubules (Franco et al., 2004; Gögel et al., 2006; Miech et al., 2008) (Figure 3I). Following the dissociation of Futsch, microtubules become destabilized and fragmented (Figure 3I), resulting in the formation of fewer boutons, which are increased in size (Franco et al., 2004; Miech et al., 2008). The protein phosphatase, calcineurin, counteracts the kinase activity of GSK-3β by dephosphorylating microtubule-associated proteins, resulting in microtubule stabilization (Figure 3I) (Gong et al., 2000a, 2000b). Because calcineurin is a Ca^{2+}/calmodulin-activated protein phosphatase (Lynch and Michalak, 2003; Rinne et al., 2009), we hypothesized that loss of Iav-dependent cytosolic Ca^{2+} elevations may result in diminished calcineurin activity, which in turn may affect microtubule stability (Figure 3I). Indeed, knocking down *Drosophila* calcineurin (*canA1*) in wild-type MNs using two RNAi lines (*UAS-canA1*^{IR} and *UAS-canA1*^{FB5}) (Dijkers and O'Farrell, 2007) results in decreased number of synaptic boutons compared to controls (Figures 4A, 4B, 4O, S2A, S2B, and S2G). Furthermore, larvae that carried the *canA1* loss-of-function allele (Nakai et al., 2011) in *trans* with a deficiency uncovering *canA1* locus (*canA1*$^{-/Df\text{-}canA1}$) exhibit decreased bouton numbers compared to the *canA1*$^{-/+}$ heterozygotes (Figures S2C, S2D, and S2G). However, MN-specific knockdown of *canA1* in *iav*^{1} does not further decrease synaptic growth (Figures 4C and 4O), suggesting that *canA1* and *iav* may function in a common pathway. Loss of CanA1 also results in an increase in bouton area (Figure S2H) and destabilization of presynaptic microtubules (Figures 4D and 4E; white arrows in Figure 4E point to fragmented tubulin within boutons). These data indicate that presynaptic loss of calcineurin decreases synaptic growth, increases the size of the boutons, and causes presynaptic microtubule destabilization at the larval NMJ—phenotypes that bear striking resemblance to those displayed by *iav*^{1}.

We also found that expression of a constitutively active CanA1, which does not require elevations in cytosolic Ca^{2+} to be fully active (*UAS-canA1*^{CA}; Dijkers and O'Farrell, 2007), in the *iav*^{1} MNs suppresses the synaptic growth defects (Figures 4F and 4P), whereas expression of CanA1^{CA} in wild-type MNs does not affect the overall bouton numbers (Figures 4G and 4P). Expression of CanA1^{CA} in the *iav*^{1} MNs also restores the bouton size (Figure S2H) and the number of Futsch loops within the NMJ boutons (Figures 4H–4K and 4Q) but does not affect the number of Futsch loops in wild-type animals (Figure 4Q). However, overexpression of CanA1^{CA} in the MNs of the *futsch* hypomorphs, *futsch*^{N94} (Roos et al., 2000), does not suppress the observed synaptic growth deficits (Figure S2I). These epistatic analyses indicate that *futsch* functions downstream of *canA1*, which in turn functions downstream of *iav*, in the regulation of synaptic growth.

Finally, if calcineurin function is decreased in *iav*^{1}, lowering the activity of the counteracting kinase, Sgg, may suppress the *iav*^{1} synaptic growth phenotype. Indeed, expression of dominant-negative *sgg* (*sgg*^{DN}) in the *iav*^{1} MNs also suppresses the synaptic growth defects (Figures 4L–4N and 4R). Together, these findings indicate that diminished calcineurin activity underlies the synaptic growth defects observed in *iav*^{1}.

ER Ca^{2+} Release Regulates NMJ Synapse Morphology and Development

Because calcineurin function is promoted by ER Ca^{2+} release (Lynch and Michalak, 2003; Rinne et al., 2009), we first assessed whether ER Ca^{2+} release plays a role in NMJ synapse development. If so, depleting the MN ER Ca^{2+} stores may alter the number and size of the NMJ boutons. Indeed, RNAi-mediated knockdown of the ER Ca^{2+} pump, SERCA (*ok371* > *serca*^{IR}), which is required for maintaining Ca^{2+} levels within the ER lumen (Dormer et al., 1993; Sanyal et al., 2005), leads to decreased synaptic growth (Figures 5A, 5B, and 5J). Similar results were obtained with *Kum*^{170}, a dominant-negative SERCA allele (Sanyal et al., 2005) (Figures 5D and 5J). Knockdown of SERCA in MNs also results in an increase in the size of NMJ boutons (Figure 5K)—morphological alterations reminiscent of the *iav*^{1} synapses.

(L–N) Confocal images of NMJs from larvae of the indicated genotypes stained with antibodies against HRP (green) and DLG (magenta). Scale bar shown in (L) also applies to (M) and (N).

(O) Quantification of the NMJ bouton number in larvae of the indicated genotypes. *p = 4.2 × 10^{-6}, one-way ANOVA, n = 12–16 NMJs per genotype.

(P) Quantification of the NMJ bouton number in larvae of the indicated genotypes. Horizontal bars above the graph indicate data from WT and *iav*^{1}. *p = 2.9 × 10^{-6}, unpaired Student's t test, n.s. represents p > 0.05, n = 16–18 NMJs per genotype

(Q) Quantification of the number of Futsch loops per NMJ in larvae of the indicated genotypes. Horizontal bars above the graph indicate data from WT and *iav*^{1}. *p = 1.8 × 10^{-6}, Student's t test, n.s. represents p > 0.05, n = 13–16 NMJs per genotype.

(R) Quantification of the NMJ bouton number in larvae of the indicated genotypes. *p = 1.4 × 10^{-6}, Student's t test, n.s. represents p > 0.05, n = 10–18 NMJs per genotype.

All values represent mean ± SEM. Abbreviations: MN, motor neuron; WT, wild-type; n.s., not significant.

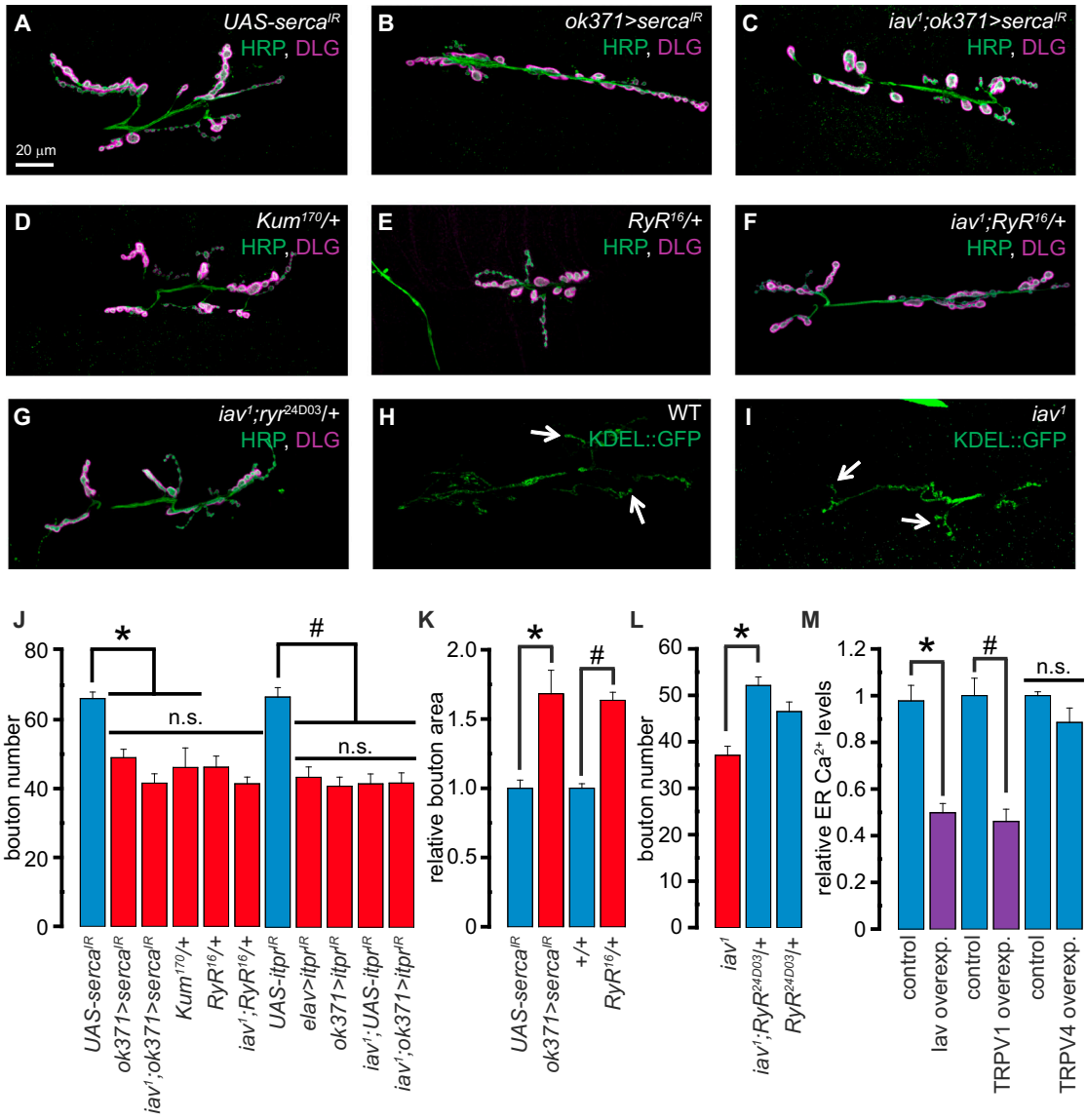

Figure 5. Role of ER Ca^{2+} Release in NMJ Synapse Development

(A–G) Confocal images of NMJs from larvae of the indicated genotypes stained with antibodies against HRP (green) and DLG (magenta).

(H and I) Confocal images of NMJs from larvae of the indicated genotypes expressing Lysozyme-KDEL::GFP (KDEL-GFP) stained with antibodies against GFP (green). Arrows point to distal boutons.

Scale bar shown in (A) also applies to (B)–(G).

(J) Quantification of the NMJ bouton numbers in larvae of the indicated genotypes. *p = 5.5×10^{-9}, one-way ANOVA (comparing the indicated data sets), n = 9–27 NMJs per genotype; #p = 1.3×10^{-8}, one-way ANOVA (comparing the indicated data sets), n = 13–14 NMJs per genotype.

(K) Quantification of the relative bouton area in larvae of the indicated genotypes. *p = 6.4×10^{-4}, unpaired Student's t test, n = 9–11 NMJs per genotype. #p = 6.2×10^{-10}, unpaired Student's t test, n = 14–16 NMJs per genotype.

(L) Quantification of the NMJ bouton numbers in larvae of the indicated genotypes. *p = 3×10^{-6}, unpaired Student's t test, n = 17–21 NMJs per genotype.

(M) Quantification of the relative ER Ca^{2+} levels as assessed by fura-2 imaging in control N2A cells and in N2A cells overexpressing (overexp.) the indicated TRPV channel. *p = 3.4×10^{-10}, unpaired Student's t test, n = 8–9 independent coverslips containing control or *iav* transfected cells (number of cells per field $\geq$ 8). #p = 4×10^{-5}, unpaired Student's t test, n = 8 independent coverslips containing control or *TRPV1* transfected cells (number of cells per field $\geq$ 10).

All values represent mean ± SEM. Abbreviations: WT, wild-type; n.s., not significant.

Next, we examined the effects of lowering ER Ca^{2+} release by decreasing the levels of the genes encoding the ER Ca^{2+} release channels, ryanodine receptor and inositol trisphosphate receptor (*RyR* and *itpr*, respectively) (Hasan and Rosbash, 1992). Loss of a single copy of *RyR* (*RyR^{16}*/+), which results in diminished ER Ca^{2+} release (Sullivan et al., 2000), leads to a decrease in the number and an increase in the size of the NMJ boutons (Figures 5E, 5J, and 5K). Similarly, presynaptic expression of

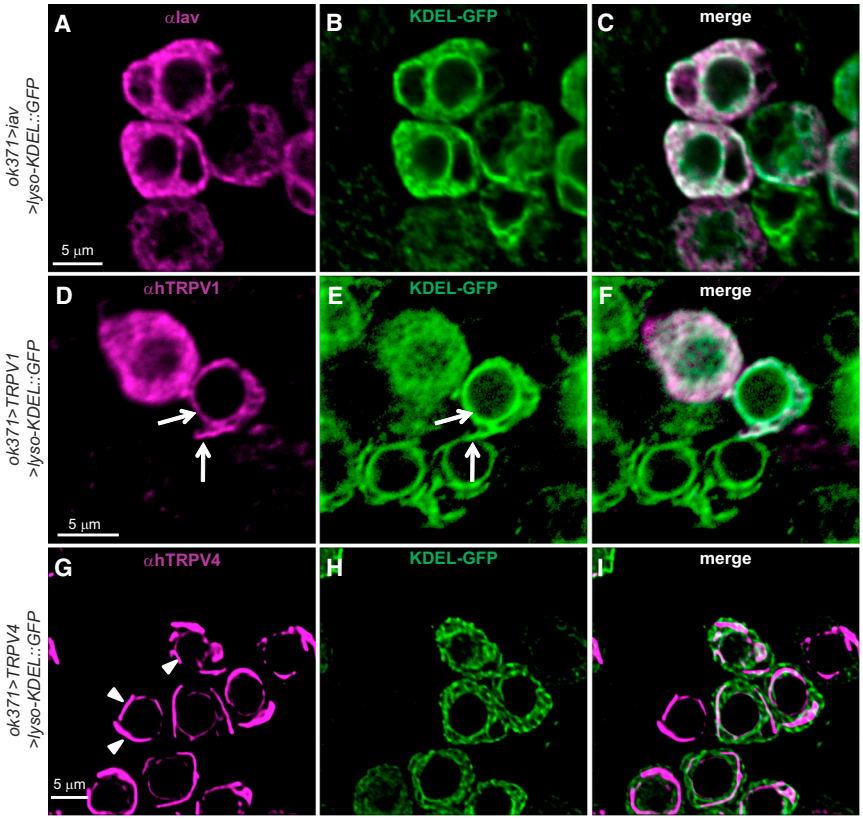

Figure 6. Subcellular Distribution of Iav, hTRPV1, and hTRPV4 in *Drosophila* Larval Motor Neurons

(A–C) Confocal images of MN cell bodies in ventral nerve cord dissected from larvae expressing Iav and KDEL-GFP in motor neurons stained with αIAV (A, magenta), αGFP (B, green), and merge (C). Scale bar shown in (A) also applies to (B) and (C).

(D–F) Same as (A)–(C), but with larvae overexpressing hTRPV1 instead of Iav. An antibody against hTRPV1 was used. Scale bar shown in (D) also applies to (E) and (F). Arrows indicate colocalization between hTRPV1 and KDEL-GFP in the nuclear envelope and other regions of the ER.

(G–I) Same as (A)–(C), but with larvae overexpressing hTRPV4 instead of Iav. An antibody against hTRPV4 was used. Scale bar shown in (G) also applies to (H) and (I). The arrowheads point to "tubular" structures that are decorated by hTRPV4 in MN cell bodies.

an RNAi against *itpr* (*UAS-itpr^{IR}*) using panneuronal or MN-specific drivers (*elav* > *itpr^{IR}* and *ok371* > *itpr^{IR}* respectively) leads to reduced NMJ bouton numbers (Figure 5J). Importantly, none of these manipulations enhance the *iav^{1}* synaptic phenotypes (Figures 5C, 5F, and 5J; n.s., $p > 0.05$, one-way ANOVA). We also asked whether promoting ER Ca^{2+} release in *iav^{1}* would suppress the synaptic growth defects. To promote ER Ca^{2+} release we used the *RyR^{24D03}*/+ flies that carry one extra copy of the *RyR* gene and exhibit elevated ER Ca^{2+} release (Gao et al., 2013). Remarkably, introduction of *RyR^{24D03}*/+ leads to a partial suppression of the *iav^{1}*-associated alterations in bouton numbers (Figures 5G and 5L). These data indicate that the *iav^{1}* synaptic growth defects arise as a result of diminished Ca^{2+} release from the ER.

Because the MN ER traverses the axons and is found at the NMJs, defects in extension of ER into the axon terminus may also result in decreased Ca^{2+} release. Thus, we evaluated ER distribution in the *iav^{1}* NMJs by expressing the ER marker Lysozyme-KDEL::GFP (using *UAS-Lyso::GFP-KDEL*; herein referred to as KDEL-GFP). Consistent with previous observations (Chouhan et al., 2010), we found that ER is distributed throughout the MN axons and is also located within some, but not all, of the synaptic boutons (Figure 5H; arrows indicate ER in distal boutons). Despite an obvious decrease in the total number of boutons, presynaptic KDEL-GFP distribution is largely unchanged in *iav^{1}* compared to controls (Figure 5I; arrows indicate ER in distal boutons). Therefore, ER trafficking to the axon terminal is not significantly altered in *iav^{1}*.

Expression of channels that promote ER Ca^{2+} release results in a partial depletion of the ER Ca^{2+} stores in cultured cells (Wegierski et al., 2009). We evaluated whether Iav, TRPV1, and TRPV4 expression in Neuro2A (N2A) cells results in lower ER Ca^{2+} levels. Expression of either Iav or TRPV1 in N2A cells results in an ~50% decrease in ER Ca^{2+} levels (Figure 5M). However, expression of TRPV4 does not affect the ER Ca^{2+} content (Figure 5M). Together, these data are consistent with a role for Iav and TRPV1 in regulating ER Ca^{2+} release, which is essential for synaptic development.

Iav and hTRPV1, but Not hTRPV4, Localize to the ER

Next, we sought to identify the subcellular distribution of Iav and TRPV1 in larval MNs. Although we could detect Iav in larval chordotonal organs using established antibodies (Gong et al., 2004) (Figure S3A), we could not detect Iav in wild-type larval MNs using these antibodies. These findings are consistent with the difficulties in observing the native expression patterns of some Ca^{2+} channels owing to their low expression levels (Ly et al., 2008; Venkatachalam et al., 2008). Therefore, we evaluated whether Iav overexpression, which suppresses the *iav^{1}* phenotypes, would reveal the protein's subcellular distribution. We found that overexpressed Iav colocalized with KDEL::GFP in MN cell bodies (Figures 6A–6C) and muscle (Figure S3B). Using anti-TRPV1 antibodies (Tominaga et al., 1998), we found that hTRPV1 also colocalizes with KDEL-GFP in the MN cell bodies (Figures 6D–6F). In contrast, hTRPV4 overexpressed in MNs does not show overlap with KDEL-GFP (Figures 6G–6I, arrowheads point to hTRPV4 expression). Hence, both Iav and hTRPV1, which suppress the NMJ defects observed in *iav^{1}*, are expressed in the ER, whereas hTRPV4, which does not suppress the *iav^{1}* NMJ growth defects, is not localized to the ER.

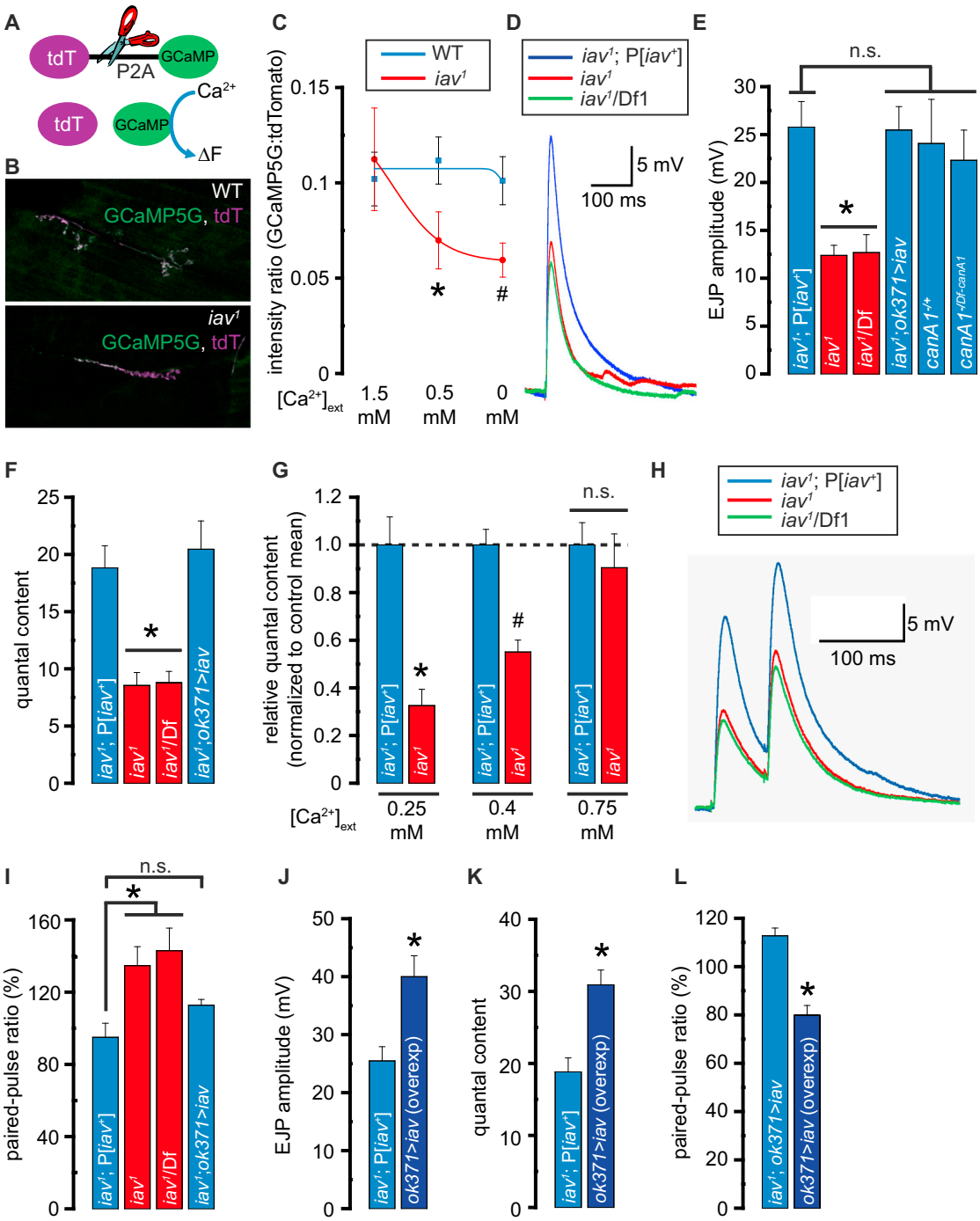

Figure 7. Diminished Presynaptic Resting Ca^{2+} Levels and Neurotransmission at the *iav*^{1} Synapses

(A) Structure of tdTomato-P2A-GCaMP5 (tdT-P2A-GCaMP). Cleavage at the P2A site (indicated by scissors) disengages the two fluorophores.

(B) Confocal images showing the expression of GCaMP5 and tdTomato (tdT) at the NMJ in larvae of the indicated genotypes.

(C) Quantification of the GCaMP5:tdTomato intensity ratios in wild-type (blue line) and *iav*^{1} (red line) at the indicated $[Ca^{2+}]_{ext}$. The blue and red curves were obtained by fitting the respective mean values to sigmoidal functions using Origin6 (OriginLab corporation). *p = 0.04, unpaired Student's t test, n = 7–8 NMJs per genotype; #p = 0.02, unpaired Student's t test, n = 7–8 NMJs per genotype.

(D) EJP traces obtained from recordings performed on larval NMJs of the indicated genotypes ($[Ca^{2+}]_{ext}$ = 0.5 mM).

(E) Quantification of the amplitude of the EJPs obtained from recordings performed on larvae of the indicated genotypes. *p = 5.1 × 10^{-4}, one-way ANOVA (comparing all the data sets shown), n = 6–8 NMJs per genotype.

(legend continued on next page)

Loss of Iav Results in Decreases in Presynaptic Resting [Ca^{2+}]

Next, we asked whether loss of Iav results in diminished cytosolic [Ca^{2+}] at NMJ termini. To evaluate resting [Ca^{2+}] within presynaptic boutons, we expressed GCaMP5G (GCaMP) (Akerboom et al., 2012) linked via a 2A peptide (P2A) to tdTomato (tdT)—a Ca^{2+}-insensitive fluorescent protein (Figure 7A) (Daniels et al., 2014). The 2A peptide is cleaved by native endoproteases in *Drosophila* neurons (Inagaki et al., 2012), leading to the separation of GCaMP5G from tdTomato—both of which are expressed at the NMJ (Figure 7B). Because the two fluorophores are translated as a single polypeptide, the levels of tdTomato can be used to normalize the levels of GCaMP5G. This ratiometric normalization is important for determining resting [Ca^{2+}], which does not involve the measurement of robust alterations from baseline. Our analysis revealed that the relative ratios of the GCaMP5G:tdTomato fluorescence intensities in WT and *iav*^{1} are comparable when the recordings are performed in extracellular bath solution containing 1.5 mM [Ca^{2+}] (Figure 7C). However, when the bath [Ca^{2+}] over the same NMJs is dropped to 0.5 mM and 0 mM, the intensity ratios show a significant decline in *iav*^{1} boutons (Figure 7C). Remarkably, the intensity ratio at WT NMJs does not change even after 9 min in a solution containing no Ca^{2+}. These data indicate that the resting cytosolic [Ca^{2+}] at NMJ bouton terminals is sustained by release of Ca^{2+} from intracellular stores and the ability of these stores to maintain presynaptic resting [Ca^{2+}] is compromised in *iav*^{1}.

Loss of Iav Results in Diminished Synaptic Transmission and SV Release Probability

We hypothesized that owing to the critical roles of presynaptic Ca^{2+} in SV release and synaptic transmission (Jahn and Fasshauer, 2012), evoked excitatory junctional potentials (EJPs) may be diminished at *iav*^{1} NMJs. Indeed, at 0.5 mM extracellular [Ca^{2+}] ([Ca^{2+}]$_{ext}$), the EJP amplitudes are ~50% lower at the *iav*^{1} NMJs compared to controls (Figures 7D and 7E). However, *canA1*-deficient NMJs, which also show a decrease in the number of synaptic boutons, do not exhibit a corresponding decrease in EJP amplitude (Figure 7E). Thus, although Iav regulates NMJ growth and morphology via calcineurin, Iav regulates synaptic transmission independent of calcineurin.

We also found that the amplitude and frequency of spontaneous mini-EJPs (mEJPs) are unchanged in *iav*^{1} (Figures S4A and S4B). Hence, the quantal content (EJP amplitude/mEJP amplitude), indicative of the number of SVs released per evoked event is ~50% decreased in *iav*^{1} (Figure 7F). The diminished EJP and quantal content in *iav*^{1} are rescued by expression of *UAS-iav* in MNs (Figures 7E and 7F).

If the decreased quantal content at *iav*^{1} NMJs is a consequence of a decrease in presynaptic resting [Ca^{2+}], raising [Ca^{2+}]$_{ext}$ during neurotransmission may restore the quantal content. To test this hypothesis, we recorded quantal contents at [Ca^{2+}]$_{ext}$ concentrations of 0.25 mM, 0.4 mM, and 0.75 mM. We found that the relative decrease in quantal content in *iav*^{1} is most severe at 0.25 mM [Ca^{2+}]$_{ext}$ (~70% lower than in controls), and becomes progressively less pronounced at higher [Ca^{2+}]$_{ext}$ (Figures S4C and 7G). At 0.75 mM [Ca^{2+}]$_{ext}$, the quantal content in *iav*^{1} is not significantly different than in controls (Figures S4C and 7G; p = 0.6, unpaired Student's t test; n = 4–5 NMJs per genotype). These data indicate that the synaptic transmission defects in *iav*^{1} are primarily a consequence of diminished presynaptic resting Ca^{2+} levels, which can be suppressed by increasing the amounts of Ca^{2+} entering the boutons through the VGCC.

Examination of the presynaptic ultrastructure by electron microscopy revealed that the *iav*^{1} NMJs do not display significant alterations in other parameters involved in regulating SV release (Figures S5A–S5C). Previous studies have found a third- to fourth-order dependence of neurotransmitter release upon [Ca^{2+}]$_{ext}$, and this cooperativity is decreased in mutations affecting the levels of the SV Ca^{2+} sensor, Synaptotagmin (Jan and Jan, 1976; Littleton et al., 1994). The Ca^{2+} cooperativity also reflects the number of VGCCs participating in the release of a single SV (Matveev et al., 2011). We found that Ca^{2+} cooperativity of neurotransmitter release in both controls and *iav*^{1} larvae, as determined by the slopes of the double-logarithmic plots of quantal content and [Ca^{2+}]$_{ext}$ (Jan and Jan, 1976; Littleton et al., 1994), remains unchanged (Figure S4C; slopes in control and *iav*^{1} are 3.4 and 3.5, respectively). Taken with the lack of alterations in SV number or distribution in *iav*^{1}, these data argue against a role for an exocytic block in the *iav*^{1} neurotransmission defects.

Cytosolic Ca^{2+} concentration at axon terminals influences SV release probability, which can be evaluated using the paired-pulse ratio of evoked potentials (Zhang et al., 2009; Zucker and Regehr, 2002). When the resting [Ca^{2+}] at a synapse is low, stimulus-induced elevation in presynaptic [Ca^{2+}] will induce the exocytosis of relatively fewer synaptic vesicles (SVs), resulting in a smaller evoked EJP. However, if a second stimulus, i.e., the paired pulse, is provided before the resting Ca^{2+} returns to baseline, the presynaptic Ca^{2+} will elevate sufficiently, leading to the exocytosis of the remaining SVs. Therefore, the higher the ratio of amplitudes of evoked responses following the first

(F) Quantification of the quantal contents obtained from recordings performed on larvae of the indicated genotypes. *p = 1.1 × 10^{-5}, one-way ANOVA (comparing all the data sets shown), n = 6–8 animals per genotype.
(G) Quantification of the relative quantal contents in *iav*^{1} normalized to the *iav*^{1}; P[*iav*$^{+}$] means at the indicated [Ca^{2+}]$_{ext}$. *p = 3.5 × 10^{-4}, unpaired Student's t test, n = 5–7 NMJs per genotype; #p = 5.3 × 10^{-5}, unpaired Student's t test, n = 7–10 NMJs per genotype.
(H) EJP trace obtained from paired-pulse recordings performed on larval NMJs of the indicated genotypes ([Ca^{2+}]$_{ext}$ = 0.5 mM).
(I) Quantification of the paired-pulse ratio (% change in the amplitude of the second EJP to that of the first EJP when the two were separated by duration of 50 ms) in the larvae of the indicated genotypes. *p = 0.01, one-way ANOVA, n = 5–7 animals per genotype.
(J) Quantification of the EJP amplitudes in larvae of the indicated genotypes. *p = 0.01, Student's t test, n = 6 NMJs per genotype.
(K) Quantification of the quantal content in larvae of the indicated genotypes. *p = 0.002, unpaired Student's t test, n = 6 NMJs per genotype.
(L) Quantification of the paired-pulse ratio in larvae of the indicated genotypes. *p = 1.5 × 10^{-4}, unpaired Student's t test, n = 5–6 NMJs per genotype.
All values represent mean ± SEM. Abbreviations: WT, wild-type; n.s., not significant.

and second pulses, respectively (known as paired pulse facilitation), the lower is the probability of SV release, and vice versa. Consistent with the observation that the *iav*^{1} NMJ synapses have reduced SV release probability, the paired-pulse ratio is increased by ~50% at *iav*^{1} NMJs (Figures 7H and 7I). Expression of *UAS-iav* in the *iav*^{1} MNs restores the SV release probability (Figure 7I).

Overexpression of Iav in Wild-Type MNs Results in Increased SV Release Probability and Neurotransmission

If Iav is a determinant of presynaptic resting Ca^{2+} levels, raising its expression level may sensitize the synapse to releasing more SVs. Indeed, overexpression of *iav* in wild-type MNs leads to a ~50% increase in EJP amplitude and quantal content (Figures 7J and 7K). We also found that the elevation in EJP amplitudes following *iav* overexpression is a consequence of increased SV release probability as determined by a decrease in the paired-pulse ratio (Figure 7L). Interestingly, overexpression of *iav* in MNs also results in the formation of fewer synaptic boutons, indicating that the number of synaptic boutons at the larval NMJ exhibits a bell-shaped dependence on the expression levels of Iav (Figure S5H). We also found that overexpression of *RyR* or *Itpr* also leads to the formation of fewer synaptic boutons at the *Drosophila* NMJ (data not shown). Thus, the consequence of *iav* overexpression on the number of synaptic boutons is likely due to an increase in presynaptic Ca^{2+} rather than a specific effect of Iav per se. However, overexpression of *iav* in the MNs does not lead to an increase in the total number of punctae formed by the active zone (AZ)-specific structural protein Bruchpilot (Brp) (Kittel et al., 2006) (Figure S5I; $p = 0.4$, unpaired Student's t test). Therefore, the increase in SV release following *iav* overexpression is a consequence of elevated resting Ca^{2+} levels rather than due to alterations in the number of SV release sites.

DISCUSSION

Iav-Mediated Calcineurin Activation Regulates Presynaptic Microtubule Stability, Bouton Morphology, and Bouton Numbers

Here we show that Iav functions in larval MNs to regulate the development and function of the NMJ. Although expression of *UAS-iav* in the *iav*^{1} MNs rescues the defects in NMJ growth and synaptic transmission, this does not alter the *iav*^{1} locomotion defects (data not shown). In contrast, expression of *UAS-iav* in the *iav*^{1} chordotonal neurons suppresses the locomotion defects (data not shown) but does not impact the NMJ phenotypes. Thus, the *iav*^{1} NMJ and proprioceptive phenotypes arise separately in the MNs and chordotonal neurons, respectively.

The phenotype of diminished synaptic bouton numbers with an increase in bouton size observed in *iav*^{1} occurs due to destabilization of presynaptic microtubules. Furthermore, our investigation revealed that in the absence of Iav, presynaptic microtubule stability, and bouton numbers are diminished due to decreased calcineurin activity. Thus, constitutively active *calcineurin* suppresses these *iav*^{1} phenotypes. However, expression of the constitutively active *calcineurin* does not suppress the synaptic growth defects in the *futsch* hypomorphs, indicating that *futsch* functions downstream of *calcineurin*. Previous studies have also implicated the other Ser/Thr protein phosphatase, PP2A, in regulating microtubule stability and NMJ development by antagonizing Sgg (Viquez et al., 2006, 2009). Because PP2A is Ca^{2+} independent, these observations suggest that distinct signals can lead to similar alterations in NMJ synapse morphology via Futsch.

The transcription factor nuclear factor of activated T cells (NFAT) is activated by calcineurin (Clipstone and Crabtree, 1992; Jain et al., 1993). However, our findings suggest the *iav*^{1} and *calcineurin* mutant phenotypes studied here are unlikely to be NFAT dependent, because NFAT knockouts display an increase in bouton number (Freeman et al., 2011) rather than the decrease observed in the *iav*^{1} and *calcineurin* mutants. Thus, in the context of NMJ synapse development, calcineurin appears to function via Futsch rather than NFAT.

Iav Regulates ER Ca^{2+} Release and Presynaptic Resting $[Ca^{2+}]$ in *Drosophila* Larval MNs

Several lines of evidence indicate that Iav and TRPV1 regulate ER Ca^{2+} release. First, decreasing ER Ca^{2+} release independent of Iav recapitulates the *iav*^{1} synaptic growth and morphological phenotypes. Moreover, loss of SERCA results in decreased EJP amplitude but normal minifrequency and amplitudes (Sanyal et al., 2005)—defects similar to those observed in *iav*^{1}. Second, elevated ER Ca^{2+} release via RyR suppresses the *iav*^{1} synaptic growth and morphological phenotypes. Third, expression of Iav or TRPV1 in N2A cells results in the partial depletion of ER stores. Fourth, overexpressed Iav and TRPV1 are localized to the ER in the MN cell bodies. Interestingly, native TRPV1 in mammalian DRG neurons have been shown to localize to the ER and also permit ER Ca^{2+} release (Castro et al., 2009; Gallego-Sandín et al., 2009), although the biological significance of TRPV1 in the ER has so far remained unknown. The ER localization of Iav and TRPV1 is not simply an artifact of overexpression of a membrane protein, because overexpressed hTRPV4 is not localized to the ER in MN cell bodies. Most importantly, Iav is required for maintaining synaptic resting $[Ca^{2+}]$ in the absence of extracellular Ca^{2+}. These data strongly support the notion that Iav regulates Ca^{2+} release from an intracellular store to maintain the presynaptic resting $[Ca^{2+}]$. Several studies have found that the ionic environment in the synaptic cleft could be tightly insulated such that $[Ca^{2+}]$ in synaptic clefts can drop dramatically during bursts of synaptic transmission, thereby severely limiting Ca^{2+} entry into the presynaptic termini (Borst and Sakmann, 1999; Egelman and Montague, 1999; Rabl and Thoreson, 2002; Rusakov and Fine, 2003; Stanley, 2000). Although the synaptic cleft in a *Drosophila* NMJ is likely permeable to extracellular ions because these synapses are not tightly insulated by glial cells (Fuentes-Medel et al., 2009), more tightly insulated synapses such as those in vertebrate CNS might be more dependent on ER Ca^{2+} release to maintain the strength of synaptic transmission during intense stimulation.

The role of Iav in maintaining presynaptic resting $[Ca^{2+}]$ is not uncovered till the extracellular $[Ca^{2+}]$ is dropped to 0.5 mM. We speculate that endogenous decreases in synaptic $[Ca^{2+}]$

to the lower end of the 0.5–1.5 mM range in *iav*^{1} might result in subthreshold activation of calcineurin. However, since the extracellular [Ca^{2+}] at a *Drosophila larval* NMJ is not known, we cannot rule out the possibility that Iav regulates the activity of calcineurin via a mechanism independent of the resting [Ca^{2+}].

Our findings also allow us to speculate that Iav could function in homeostatic control of presynaptic [Ca^{2+}]. The activity of Iav may be suppressed at resting [Ca^{2+}] via proteins such as calmodulin such that a drop in resting [Ca^{2+}] could result in Iav disinhibition and channel opening. Indeed, ER Ca^{2+} release via TRPV1 has been shown to be strongly suppressed by calmodulin binding to a C-terminal calmodulin binding domain on TRPV1 (Gallego-Sandín et al., 2009). Interestingly, Iav also contains a C-terminal calmodulin binding domain, which may underlie the homeostatic control of Iav activity.

Evoked Neurotransmission at the *Drosophila* Larval NMJ Depends on Iav Dosage and Presynaptic [Ca^{2+}] Rather Than the Number of Release Sites

Owing to its function in the regulation of presynaptic resting [Ca^{2+}], Iav influences SV release probability and the amplitude of evoked neurotransmission without affecting the Ca^{2+} cooperativity of SV release. Furthermore, Iav regulates neurotransmission in a dose-dependent manner consistent with a critical function of the protein in evoked neurotransmission. Although calcineurin inhibits SV cycling at the *Drosophila* NMJ (Kuromi et al., 1997) and promotes synaptic growth, calcineurin does not play a role in Iav-dependent regulation of synaptic transmission. Moreover, our findings indicate that presynaptic Ca^{2+}, rather than the number of SV release sites, is the major factor in regulating the evoked SV release. Thus, at higher extracellular [Ca^{2+}], the Ca^{2+} entering via the VGCC compensates for the lower resting [Ca^{2+}] in *iav*^{1}, thereby resulting in normal synaptic transmission despite the reduction in the number of NMJ boutons and AZs (number of Brp punctae per NMJ, *iav*^{1};P[*iav*$^{+}$] = 413.1, *iav*^{1} = 339.4, p = 0.01, Student's t test, n = 11 NMJs per genotype). Thus, synaptic transmission does not change proportionally with the number of synaptic boutons or even the number of AZs per synapse. Indeed, only ~50% of AZs at a *Drosophila* larval NMJ participate in SV release (Peled and Isacoff, 2011), and although both *vapb* and *futsch* mutants have fewer synaptic boutons, they exhibit elevated evoked synaptic transmission (Chai et al., 2008; Zhang et al., 2001).

EXPERIMENTAL PROCEDURES

Immunohistochemistry and Confocal Imaging

Wandering third-instar larvae were filleted in ice-cold PBS by cutting the body wall open along the dorsal midline and removing the visceral organs except the brain and nerves. The fillet was fixed in 4% PFA in PBS for 30 min. The fixed fillets were washed with 0.1% Triton X-100 in PBS before incubation with primary antibodies overnight at 4°C. Antibody dilutions were as follows: 1:200 rabbit anti-HRP (Jackson ImmunoResearch), 1:100 mouse anti-DLG (Parnas et al., 2001), 1:50 mouse anti-NC82 (Wagh et al., 2006), 1:50 mouse anti-Futsch (Fujita et al., 1982), 1:100 mouse anti-α-tubulin (Thazhath et al., 2002), 1:200 mouse anti-GFP (Invitrogen), 1:200 rabbit anti-TRPV1 and anti-TRPV4 (Alomone Labs), and 1:200 GFP-Booster (Chromotek). The rat anti-Iav antibody (anti-serum GNIEb; Gong et al., 2004) was precleared by incubating the antibody with fixed *iav*^{1} fillets at a concentration of 1:100. Subsequently, the precleared antibody was used at dilution of 1:5. The monoclonal antibodies against DLG, NC82, Futsch, and α-tubulin were obtained from the Developmental Studies Hybridoma Bank developed under the auspices of the NICHD and maintained by The University of Iowa, Department of Biology, Iowa City, IA 52242. The samples were then washed and probed with fluorophore-conjugated secondary antibodies (1:400, Alexa Fluor 488/568/647) (Invitrogen) at room temperature for 1.5 hr and then mounted on glass slides with Vectashield (Vector Labs). Confocal images were obtained using a Nikon A1 Confocal Laser Microscope System (Nikon). For NMJ bouton counting, a 60× oil objective was used to focus on the NMJs on abdominal segment 3.

Evaluation of NMJ Presynaptic [Ca^{2+}] Using tdTomato-P2A-GCaMP5G

Third-instar larval fillets were prepared in ice-cold HL-3.1, which contained (in mM): 70 NaCl, 5 KCl, 1.5 $CaCl_2$, 4 $MgCl_2$, 10 $NaHCO_3$, 5 trehelose, 115 sucrose, and 5 HEPES. A total of 7 mM L-glutamic acid was added to HL-3.1 to desensitize glutamate receptors and prevent muscle contraction during the course of experiment. The VNCs was severed from the dorsal brain lobes to prevent peristalsis. Dissected fillets were allowed to equilibrate to room temperature in HL3.1 containing 1.5 mM Ca^{2+} for at least 15 min before imaging. Type 1b boutons on muscle M13 of abdominal segment A4 were brought to focus with a 100× water-immersion objective on an Olympus BX51WI microscope. Images were captured with an Andor Technology EMCCD camera (DU860) under the control of Ando IQ software. Subsequently, fluorescence signals were captured for tdTomato and for GCaMP5G. The bath solution was then exchanged to HL3.1 containing 0.5 mM $CaCl_2$. Two minutes after bath exchange, fluorescence signals were captured at the same settings. Bath solution was then further exchanged to nominally Ca^{2+} free HL3.1. Fluorescence signals were then captured again 2 min and 9 min after bath exchange. Recorded images were analyzed using Andor IQ software. Regions not containing an axon terminal and close to a region of interest (ROI) were selected as background. Average pixel intensity from the background regions was subtracted from that of ROI for each fluorescence channel.

Ca^{2+} Imaging in N2A Cells

N2A cells were cultured in DMEM (Invitrogen) supplemented with 5% fetal bovine serum. Cells were transfected with *TRPV* cDNA or control vector using X-tremeGENE 9 DNA transfection reagent (Roche) at 1:4 DNA-to-reagent ratio according to the manufacturer's instructions. One day later, transfected cells were trypsinized and seeded onto poly-D-lysine-coated glass coverslips. Another day later, cells were loaded with 10 μM fura2-AM (Invitrogen) in culture medium for 30 min. The glass coverslips were mounted onto a chamber containing 500 μl of bath solution (125 mM NaCl, 5 mM KCl, 10 mM $MgSO_4$, 10 mM KH_2PO_4, 1 mM $CaCl_2$, 5.5 mM glucose, and 5 mM HEPES [pH 7.4]). Fura-2 signals, which represent cytosolic free [Ca^{2+}], were recorded by 340/380 nm excitation and 510 nm emission, using a TiE Wide-Field Fluorescence Imaging System (Nikon). The background-subtracted emission ratio ($R_{340/380}$) was measured and calculated by NIS Elements imaging software (Nikon).

To evaluate the total ER Ca^{2+} content, we completely released the ER Ca^{2+} stores using thapsigargin (TG) while simultaneously evaluating the resulting elevation in cytosolic Ca^{2+}, which is indicative of the total ER Ca^{2+} levels (Wegierski et al., 2009). Baseline fura-2 fluorescence was first acquired for 1 min, before replacing the bath solution with Ca^{2+}-free bath solution. Three minutes after removing bath Ca^{2+}, 5 μM TG was added to the bath, and the fluorescence images were recorded for another 6 min. The amplitude of the $R_{340/380}$ was taken to be the total ER Ca^{2+} content of those cells.

SUPPLEMENTAL INFORMATION

Supplemental Information includes Supplemental Experimental Procedures, one table, and five figures and can be found with this article at http://dx.doi.org/10.1016/j.neuron.2014.09.030.

ACKNOWLEDGMENTS

We thank the Bloomington *Drosophila* Stock Center for fly stocks, Dr. C. Montell for the *trpg*^{G4} and *UAS-nan* flies, Dr. T. Aigaki for the *canA1*-deficient flies, Dr. S. Sanyal for the *kum*^{170} flies, Dr. P. O'Farrell for the *UAS-canA1*^{FB5} and *UAS-canA1*^{CA} lines, Drs. D. Sandstrom and B. White for the *RyR*^{24D03} flies, Dr. C. Kim for the anti-lav antibodies, and Dr. R. Daniels for the *UAS-tdTomato-P2A-GCaMP5G* flies. We also thank Dr. C.-K. Yao and H. Hu for technical help. We are grateful to N. Haelterman, Dr. N. Giagtzoglou, Dr. S. Yamamoto, Dr. H. Sandoval, and Dr. M. Jaiswal for helpful discussions. H.J.B. is an Investigator of the HHMI. This work was supported by the NINDS grant R01NS081301 (to K.V.).

Accepted: September 10, 2014
Published: October 30, 2014

REFERENCES

Akerboom, J., Chen, T.W., Wardill, T.J., Tian, L., Marvin, J.S., Mutlu, S., Calderón, N.C., Esposti, F., Borghuis, B.G., Sun, X.R., et al. (2012). Optimization of a GCaMP calcium indicator for neural activity imaging. J. Neurosci. *32*, 13819–13840.

Awatramani, G.B., Price, G.D., and Trussell, L.O. (2005). Modulation of transmitter release by presynaptic resting potential and background calcium levels. Neuron *48*, 109–121.

Borst, J.G., and Sakmann, B. (1999). Depletion of calcium in the synaptic cleft of a calyx-type synapse in the rat brainstem. J. Physiol. *521*, 123–133.

Castro, J., Aromataris, E.C., Rychkov, G.Y., and Barritt, G.J. (2009). A small component of the endoplasmic reticulum is required for store-operated Ca2+ channel activation in liver cells: evidence from studies using TRPV1 and taurodeoxycholic acid. Biochem. J. *418*, 553–566.

Caterina, M.J., Rosen, T.A., Tominaga, M., Brake, A.J., and Julius, D. (1999). A capsaicin-receptor homologue with a high threshold for noxious heat. Nature *398*, 436–441.

Caterina, M.J., Leffler, A., Malmberg, A.B., Martin, W.J., Trafton, J., Petersen-Zeitz, K.R., Koltzenburg, M., Basbaum, A.I., and Julius, D. (2000). Impaired nociception and pain sensation in mice lacking the capsaicin receptor. Science *288*, 306–313.

Catterall, W.A. (2000). Structure and regulation of voltage-gated Ca2+ channels. Annu. Rev. Cell Dev. Biol. *16*, 521–555.

Chai, A., Withers, J., Koh, Y.H., Parry, K., Bao, H., Zhang, B., Budnik, V., and Pennetta, G. (2008). hVAPB, the causative gene of a heterogeneous group of motor neuron diseases in humans, is functionally interchangeable with its Drosophila homologue DVAP-33A at the neuromuscular junction. Hum. Mol. Genet. *17*, 266–280.

Cho, K.O., Hunt, C.A., and Kennedy, M.B. (1992). The rat brain postsynaptic density fraction contains a homolog of the *Drosophila* discs-large tumor suppressor protein. Neuron *9*, 929–942.

Chouhan, A.K., Zhang, J., Zinsmaier, K.E., and Macleod, G.T. (2010). Presynaptic mitochondria in functionally different motor neurons exhibit similar affinities for Ca2+ but exert little influence as Ca2+ buffers at nerve firing rates in situ. J. Neurosci. *30*, 1869–1881.

Clipstone, N.A., and Crabtree, G.R. (1992). Identification of calcineurin as a key signalling enzyme in T-lymphocyte activation. Nature *357*, 695–697.

Daniels, R.W., Rossano, A.J., Macleod, G.T., and Ganetzky, B. (2014). Expression of multiple transgenes from a single construct using viral 2A peptides in Drosophila. PLoS ONE *9*, e100637.

Dijkers, P.F., and O'Farrell, P.H. (2007). Drosophila calcineurin promotes induction of innate immune responses. Curr. Biol. *17*, 2087–2093.

Dormer, R.L., Capurro, D.E., Morris, R., and Webb, R. (1993). Demonstration of two isoforms of the SERCA-2b type Ca2+,Mg(2+)-ATPase in pancreatic endoplasmic reticulum. Biochim. Biophys. Acta *1152*, 225–230.

Egelman, D.M., and Montague, P.R. (1999). Calcium dynamics in the extracellular space of mammalian neural tissue. Biophys. J. *76*, 1856–1867.

Fowler, M.A., and Montell, C. (2013). Drosophila TRP channels and animal behavior. Life Sci. *92*, 394–403.

Franco, B., Bogdanik, L., Bobinnec, Y., Debec, A., Bockaert, J., Parmentier, M.L., and Grau, Y. (2004). Shaggy, the homolog of glycogen synthase kinase 3, controls neuromuscular junction growth in Drosophila. J. Neurosci. *24*, 6573–6577.

Freeman, A., Franciscovich, A., Bowers, M., Sandstrom, D.J., and Sanyal, S. (2011). NFAT regulates pre-synaptic development and activity-dependent plasticity in Drosophila. Mol. Cell. Neurosci. *46*, 535–547.

Fuentes-Medel, Y., Logan, M.A., Ashley, J., Ataman, B., Budnik, V., and Freeman, M.R. (2009). Glia and muscle sculpt neuromuscular arbors by engulfing destabilized synaptic boutons and shed presynaptic debris. PLoS Biol. *7*, e1000184.

Fujita, S.C., Zipursky, S.L., Benzer, S., Ferrús, A., and Shotwell, S.L. (1982). Monoclonal antibodies against the Drosophila nervous system. Proc. Natl. Acad. Sci. USA *79*, 7929–7933.

Gallego-Sandín, S., Rodríguez-García, A., Alonso, M.T., and García-Sancho, J. (2009). The endoplasmic reticulum of dorsal root ganglion neurons contains functional TRPV1 channels. J. Biol. Chem. *284*, 32591–32601.

Gao, S., Sandstrom, D.J., Smith, H.E., High, B., Marsh, J.W., and Nash, H.A. (2013). Drosophila ryanodine receptors mediate general anesthesia by halothane. Anesthesiology *118*, 587–601.

Gögel, S., Wakefield, S., Tear, G., Klämbt, C., and Gordon-Weeks, P.R. (2006). The Drosophila microtubule associated protein Futsch is phosphorylated by Shaggy/Zeste-white 3 at an homologous GSK3beta phosphorylation site in MAP1B. Mol. Cell. Neurosci. *33*, 188–199.

Gong, C.X., Lidsky, T., Wegiel, J., Zuck, L., Grundke-Iqbal, I., and Iqbal, K. (2000a). Phosphorylation of microtubule-associated protein tau is regulated by protein phosphatase 2A in mammalian brain. Implications for neurofibrillary degeneration in Alzheimer's disease. J. Biol. Chem. *275*, 5535–5544.

Gong, C.X., Wegiel, J., Lidsky, T., Zuck, L., Avila, J., Wisniewski, H.M., Grundke-Iqbal, I., and Iqbal, K. (2000b). Regulation of phosphorylation of neuronal microtubule-associated proteins MAP1b and MAP2 by protein phosphatase-2A and -2B in rat brain. Brain Res. *853*, 299–309.

Gong, Z., Son, W., Chung, Y.D., Kim, J., Shin, D.W., McClung, C.A., Lee, Y., Lee, H.W., Chang, D.J., Kaang, B.K., et al. (2004). Two interdependent TRPV channel subunits, inactive and Nanchung, mediate hearing in *Drosophila*. J. Neurosci. *24*, 9059–9066.

Güler, A.D., Lee, H., Iida, T., Shimizu, I., Tominaga, M., and Caterina, M. (2002). Heat-evoked activation of the ion channel, TRPV4. J. Neurosci. *22*, 6408–6414.

Hasan, G., and Rosbash, M. (1992). Drosophila homologs of two mammalian intracellular Ca(2+)-release channels: identification and expression patterns of the inositol 1,4,5-triphosphate and the ryanodine receptor genes. Development *116*, 967–975.

Inagaki, H.K., Ben-Tabou de-Leon, S., Wong, A.M., Jagadish, S., Ishimoto, H., Barnea, G., Kitamoto, T., Axel, R., and Anderson, D.J. (2012). Visualizing neuromodulation in vivo: TANGO-mapping of dopamine signaling reveals appetite control of sugar sensing. Cell *148*, 583–595.

Jahn, R., and Fasshauer, D. (2012). Molecular machines governing exocytosis of synaptic vesicles. Nature *490*, 201–207.

Jain, J., McCaffrey, P.G., Miner, Z., Kerppola, T.K., Lambert, J.N., Verdine, G.L., Curran, T., and Rao, A. (1993). The T-cell transcription factor NFATp is a substrate for calcineurin and interacts with Fos and Jun. Nature *365*, 352–355.

Jan, L.Y., and Jan, Y.N. (1976). Properties of the larval neuromuscular junction in Drosophila melanogaster. J. Physiol. *262*, 189–214.

Kim, J., Chung, Y.D., Park, D.Y., Choi, S., Shin, D.W., Soh, H., Lee, H.W., Son, W., Yim, J., Park, C.S., et al. (2003). A TRPV family ion channel required for hearing in *Drosophila*. Nature *424*, 81–84.

Kittel, R.J., Wichmann, C., Rasse, T.M., Fouquet, W., Schmidt, M., Schmid, A., Wagh, D.A., Pawlu, C., Kellner, R.R., Willig, K.I., et al. (2006). Bruchpilot

promotes active zone assembly, Ca2+ channel clustering, and vesicle release. Science *312*, 1051–1054.

Kuromi, H., Yoshihara, M., and Kidokoro, Y. (1997). An inhibitory role of calcineurin in endocytosis of synaptic vesicles at nerve terminals of Drosophila larvae. Neurosci. Res. *27*, 101–113.

Kuzmenkin, A., Bezanilla, F., and Correa, A.M. (2004). Gating of the bacterial sodium channel, NaChBac: voltage-dependent charge movement and gating currents. J. Gen. Physiol. *124*, 349–356.

Littleton, J.T., Stern, M., Perin, M., and Bellen, H.J. (1994). Calcium dependence of neurotransmitter release and rate of spontaneous vesicle fusions are altered in Drosophila synaptotagmin mutants. Proc. Natl. Acad. Sci. USA *91*, 10888–10892.

Luan, H., Lemon, W.C., Peabody, N.C., Pohl, J.B., Zelensky, P.K., Wang, D., Nitabach, M.N., Holmes, T.C., and White, B.H. (2006). Functional dissection of a neuronal network required for cuticle tanning and wing expansion in Drosophila. J. Neurosci. *26*, 573–584.

Ly, C.V., Yao, C.K., Verstreken, P., Ohyama, T., and Bellen, H.J. (2008). straightjacket is required for the synaptic stabilization of cacophony, a voltage-gated calcium channel alpha1 subunit. J. Cell Biol. *181*, 157–170.

Lynch, J., and Michalak, M. (2003). Calreticulin is an upstream regulator of calcineurin. Biochem. Biophys. Res. Commun. *311*, 1173–1179.

Matveev, V., Bertram, R., and Sherman, A. (2011). Calcium cooperativity of exocytosis as a measure of Ca^2+ channel domain overlap. Brain Res. *1398*, 126–138.

Miech, C., Pauer, H.U., He, X., and Schwarz, T.L. (2008). Presynaptic local signaling by a canonical wingless pathway regulates development of the Drosophila neuromuscular junction. J. Neurosci. *28*, 10875–10884.

Nakai, Y., Horiuchi, J., Tsuda, M., Takeo, S., Akahori, S., Matsuo, T., Kume, K., and Aigaki, T. (2011). Calcineurin and its regulator sra/DSCR1 are essential for sleep in Drosophila. J. Neurosci. *31*, 12759–12766.

Nishimura, A.L., Mitne-Neto, M., Silva, H.C., Richieri-Costa, A., Middleton, S., Cascio, D., Kok, F., Oliveira, J.R., Gillingwater, T., Webb, J., et al. (2004). A mutation in the vesicle-trafficking protein VAPB causes late-onset spinal muscular atrophy and amyotrophic lateral sclerosis. Am. J. Hum. Genet. *75*, 822–831.

Packard, M., Koo, E.S., Gorczyca, M., Sharpe, J., Cumberledge, S., and Budnik, V. (2002). The Drosophila Wnt, wingless, provides an essential signal for pre- and postsynaptic differentiation. Cell *111*, 319–330.

Parnas, D., Haghighi, A.P., Fetter, R.D., Kim, S.W., and Goodman, C.S. (2001). Regulation of postsynaptic structure and protein localization by the Rho-type guanine nucleotide exchange factor dPix. Neuron *32*, 415–424.

Peled, E.S., and Isacoff, E.Y. (2011). Optical quantal analysis of synaptic transmission in wild-type and rab3-mutant Drosophila motor axons. Nat. Neurosci. *14*, 519–526.

Pennetta, G., Hiesinger, P.R., Fabian-Fine, R., Meinertzhagen, I.A., and Bellen, H.J. (2002). Drosophila VAP-33A directs bouton formation at neuromuscular junctions in a dosage-dependent manner. Neuron *35*, 291–306.

Rabl, K., and Thoreson, W.B. (2002). Calcium-dependent inactivation and depletion of synaptic cleft calcium ions combine to regulate rod calcium currents under physiological conditions. Eur. J. Neurosci. *16*, 2070–2077.

Rinne, A., Banach, K., and Blatter, L.A. (2009). Regulation of nuclear factor of activated T cells (NFAT) in vascular endothelial cells. J. Mol. Cell. Cardiol. *47*, 400–410.

Roos, J., Hummel, T., Ng, N., Klämbt, C., and Davis, G.W. (2000). Drosophila Futsch regulates synaptic microtubule organization and is necessary for synaptic growth. Neuron *26*, 371–382.

Rusakov, D.A., and Fine, A. (2003). Extracellular Ca2+ depletion contributes to fast activity-dependent modulation of synaptic transmission in the brain. Neuron *37*, 287–297.

Sanyal, S., Consoulas, C., Kuromi, H., Basole, A., Mukai, L., Kidokoro, Y., Krishnan, K.S., and Ramaswami, M. (2005). Analysis of conditional paralytic mutants in Drosophila sarco-endoplasmic reticulum calcium ATPase reveals novel mechanisms for regulating membrane excitability. Genetics *169*, 737–750.

Snow, P.M., Patel, N.H., Harrelson, A.L., and Goodman, C.S. (1987). Neural-specific carbohydrate moiety shared by many surface glycoproteins in Drosophila and grasshopper embryos. J. Neurosci. *7*, 4137–4144.

Stanley, E.F. (2000). Presynaptic calcium channels and the depletion of synaptic cleft calcium ions. J. Neurophysiol. *83*, 477–482.

Sullivan, K.M., Scott, K., Zuker, C.S., and Rubin, G.M. (2000). The ryanodine receptor is essential for larval development in Drosophila melanogaster. Proc. Natl. Acad. Sci. USA *97*, 5942–5947.

Thazhath, R., Liu, C., and Gaertig, J. (2002). Polyglycylation domain of beta-tubulin maintains axonemal architecture and affects cytokinesis in Tetrahymena. Nat. Cell Biol. *4*, 256–259.

Tominaga, M., Caterina, M.J., Malmberg, A.B., Rosen, T.A., Gilbert, H., Skinner, K., Raumann, B.E., Basbaum, A.I., and Julius, D. (1998). The cloned capsaicin receptor integrates multiple pain-producing stimuli. Neuron *21*, 531–543.

Venkatachalam, K., and Montell, C. (2007). TRP channels. Annu. Rev. Biochem. *76*, 387–417.

Venkatachalam, K., Long, A.A., Elsaesser, R., Nikolaeva, D., Broadie, K., and Montell, C. (2008). Motor deficit in a *Drosophila* model of mucolipidosis type IV due to defective clearance of apoptotic cells. Cell *135*, 838–851.

Viquez, N.M., Li, C.R., Wairkar, Y.P., and DiAntonio, A. (2006). The B' protein phosphatase 2A regulatory subunit well-rounded regulates synaptic growth and cytoskeletal stability at the Drosophila neuromuscular junction. J. Neurosci. *26*, 9293–9303.

Viquez, N.M., Füger, P., Valakh, V., Daniels, R.W., Rasse, T.M., and DiAntonio, A. (2009). PP2A and GSK-3beta act antagonistically to regulate active zone development. J. Neurosci. *29*, 11484–11494.

Wagh, D.A., Rasse, T.M., Asan, E., Hofbauer, A., Schwenkert, I., Dürrbeck, H., Buchner, S., Dabauvalle, M.C., Schmidt, M., Qin, G., et al. (2006). Bruchpilot, a protein with homology to ELKS/CAST, is required for structural integrity and function of synaptic active zones in Drosophila. Neuron *49*, 833–844.

Watanabe, H., Davis, J.B., Smart, D., Jerman, J.C., Smith, G.D., Hayes, P., Vriens, J., Cairns, W., Wissenbach, U., Prenen, J., et al. (2002). Activation of TRPV4 channels (hVRL-2/mTRP12) by phorbol derivatives. J. Biol. Chem. *277*, 13569–13577.

Wegierski, T., Steffl, D., Kopp, C., Tauber, R., Buchholz, B., Nitschke, R., Kuehn, E.W., Walz, G., and Köttgen, M. (2009). TRPP2 channels regulate apoptosis through the Ca2+ concentration in the endoplasmic reticulum. EMBO J. *28*, 490–499.

Xia, R., Dekermendjian, K., Lullau, E., and Dekker, N. (2011a). TRPV1: a therapy target that attracts the pharmaceutical interests. Adv. Exp. Med. Biol. *704*, 637–665.

Xia, R., Samad, T.A., Btesh, J., Jiang, L.H., Kays, I., Stjernborg, L., and Dekker, N. (2011b). TRPV1 signaling: mechanistic understanding and therapeutic potential. Curr. Top. Med. Chem. *11*, 2180–2191.

Zhang, Y.Q., Bailey, A.M., Matthies, H.J., Renden, R.B., Smith, M.A., Speese, S.D., Rubin, G.M., and Broadie, K. (2001). *Drosophila* fragile X-related gene regulates the MAP1B homolog Futsch to control synaptic structure and function. Cell *107*, 591–603.

Zhang, C., Wu, B., Beglopoulos, V., Wines-Samuelson, M., Zhang, D., Dragatsis, I., Südhof, T.C., and Shen, J. (2009). Presenilins are essential for regulating neurotransmitter release. Nature *460*, 632–636.

Zucker, R.S., and Regehr, W.G. (2002). Short-term synaptic plasticity. Annu. Rev. Physiol. *64*, 355–405.

Zygmunt, P.M., Petersson, J., Andersson, D.A., Chuang, H., Sørgård, M., Di Marzo, V., Julius, D., and Högestätt, E.D. (1999). Vanilloid receptors on sensory nerves mediate the vasodilator action of anandamide. Nature *400*, 452–457.

Neuron, Volume *84*

Supplemental Information

A TRPV Channel in *Drosophila* Motor Neurons Regulates Presynaptic Resting Ca^{2+} Levels, Synapse Growth, and Synaptic Transmission

Ching-On Wong, Kuchuan Chen, Yong Qi Lin, Yufang Chao, Lita Duraine, Zhongmin Lu, Wan Hee Yoon, Jeremy M. Sullivan, Geoffrey T. Broadhead, Charlotte J. Sumner, Thomas E. Lloyd, Gregory T. Macleod, Hugo J. Bellen, and Kartik Venkatachalam

SUPPLEMENTAL EXPERIMENTAL PROCEDURES

Drosophila strains

The existing strains used in the study were *Canton-S*, w^{1118}, iav^{1} (Gong et al., 2004), iav^{3621} (Gong et al., 2004), iav^{1}; P[iav^{+}] (Gong et al., 2004), *Df(1)BSC276 /FM7h/Dp(2;Y)G*, *Y* (Df1) (Bloomington *Drosophila* Stock Center), *Df(1)ED6878 /FM7h* (Df2) (Bloomington *Drosophila* Stock Center), *Df(3L)Exel6120, P{XP-U}Exel6120*/*TM6B, Tb*^{1} (Df^{nan}) (Bloomington *Drosophila* Stock Center), *UAS-iav* (Kwon et al., 2010), *UAS-nan* (kind gift from Dr. Craig Montell, UCSB), *UAS-iav*$^{IR(JF01904)}$ (Bloomington *Drosophila* Stock Center), *ok371-GAL4* (Brand and Perrimon, 1993; Meyer and Aberle, 2006), *d42-GAL4* (Sweeney and Davis, 2002), *n-syb-GAL4* (Pauli et al., 2008), *mef2-GAL4* (Ranganayakulu et al., 1996), *ato-GAL4* (Hassan et al., 2000), *UAS-NaChBac* (Luan et al., 2006), *UAS-hTRPV1* (Marella et al., 2006), *UAS-lysozyme-KDEL::GFP* (Snapp et al., 2004), kum^{170} (Sanyal et al., 2005), *UAS-serca*$^{IR(JF01948)}$ (Bloomington *Drosophila* Stock Center), RyR^{16} (Sullivan et al., 2000), *UAS-itpr*$^{IR(JF01957)}$ (Bloomington *Drosophila* Stock Center), RyR^{24D03} (Gao et al., 2013), *canA1*$^{KO2-2}$ (*canA1*$^{-/-}$, (Nakai et al., 2011)), *UAS-canA1*$^{IR(JF01871)}$ (Bloomington *Drosophila* Stock Center), *UAS-canA1*^{FB5} (Dijkers and O'Farrell, 2007), *UAS-canA1*^{CA} (Dijkers and O'Farrell, 2007), *UAS-sgg*^{DN} (Bourouis, 2002), nan^{36a} (Kim et al., 2003), trp^{1} (Montell et al., 1985), *trpγ*^{G4} (kind gift from Dr. Craig Montell, UCSB), $trpL^{302}$ (Niemeyer et al., 1996), *pain*^{GAL4} (Tracey et al., 2003), pyx^{3} (Lee et al., 2005), $trpA1^{1}$ (Kwon et al., 2008), $wtrw^{2}$ (Kwon et al., 2008), *futsch*^{N94} (Roos et al., 2000).

The iav^{1} allele was previously attributed to a premature STOP codon in the *iav* gene (C1363T leading to Q455X) (Gong et al., 2004). However, when we resequenced the

iav^{1} genomic DNA, we found that the actual mutation in the *iav* gene is C908T. We found that C1363 is not mutated in *iav*^{1}. Nevertheless, the lack of Iav protein in the *iav*^{1} chordotonal neurons (Figure S3A) indicates that this newly identified mutation also leads to the absence of Iav protein as described (Gong et al., 2004).

Fly husbandry and chemical feeding

All flies were reared at room temperature (~22°C). Except for the experiments with capsazepine feeding, all flies were raised in standard fly food (1 L of liquid fly food contained: 95 g agar, 275 g Brewer's yeast, 520 g of cornmeal, 110 g of sugar, 45 g of propionic acid, and 36 g of Tegosept was dissolved in 92 ml of 95% ethanol). For the drug feeding experiments, 2.5 g of instant fly food (formula 4-24 plain, Carolina Biological Supply Company) with an additional 0.5 g of inactive yeast was suspended in 6 mL water with capsazepine or the vehicle solvent (methanol (1% v/v)).

Image quantification

In some analyses, Z-series were exported as TIFF files into the Image-Pro Plus software (Media Cybernetics) for deconvolution and 3-dimensional reconstructions. Bouton volumes were determined after 3D reconstruction using available functions in Image-Pro Plus. For determining the area of the synaptic boutons, the total area stained by DLG was divided by the number of boutons at that NMJ. In the data shown in Figures 4G-4H, an "HRP-mask" was applied by isolating the signal of the relevant channel that overlapped with HRP using Image-Pro Plus.

NMJ Electrophysiology

NMJ electrophysiology was performed as described previously (Yao et al., 2009). Briefly, wandering third instar larvae were dissected in ice-cold, zero calcium HL-3 (70 mM NaCl, 5 mM KCl, 20 mM $MgCl_2$, 10 mM $NaHCO_3$, 115 mM sucrose, 5 mM trehalose, and 5 mM HEPES; pH 7.2.), and rinsed with HL-3 containing indicated Ca^{2+} concentration. The fillet was incubated in the latter solution for at least 3 minutes before recording. Recordings were made from body-wall muscles 6 (abdominal segment 3) with sharp electrodes filled with a 2:1 mixture of 2 M potassium acetate and 2 M potassium chloride. Data were collected only when resting membrane potential was below −60 mV. EJPs were evoked by directly stimulating the hemisegmental nerve through a glass capillary electrode (internal diameter, ~10 μm) at 0.2 Hz. Stimulus pulses were generated by pClamp 8 software (Axon Instruments Inc). The applied currents were 6 μA ± 3 with fixed stimulus duration at 0.3 ms. Twenty to thirty evoked EJPs were recorded for each muscle for analysis. Miniature EJP (mEJP) events were collected for 5 min. Both EJPs and mEJPs were amplified with an Axoclamp 2B amplifier (Axon Instruments, Foster City, CA) under bridge mode, filtered at 10 kHz and digitized at 10 kHz (for EJPs) and 40 kHz (mEJPs) respectively with pClamp 8.0. Experiments were performed at room temperature (20°C – 22°C).

EJPs and paired-pulse stimulation were analyzed with pClamp 8.0 software (Axon Instruments). The mEJPs were analyzed using the Mini Analysis Program (Synaptosoft Inc., Decatur, GA). The EJPs amplitudes were corrected by nonlinear summation (Feeney et al., 1998). The quantal content of evoked release was calculated from individual muscles by the ratio of the average EJP amplitude over the average mEJP

amplitude. The Ca^{2+} cooperativity of neurotransmission was calculated as described (Jan and Jan, 1976; Littleton et al., 1994).

Transmission electron microscopy

NMJ ultrastructural imaging was done as described previously (Yao et al., 2009). Briefly, wandering third instar larvae were filleted at room temperature in Ca^{2+} free HL-3 medium and subsequently fixed overnight in 2% paraformaldehyde/2.5% glutaraldehyde/0.1 M cacodylic acid (pH 7.2). The pre-fixed fillets were then processed inside a Ted Pella Bio Wave microwave with vacuum attachments. Samples were fixed again, followed by 3x water rinses, post-fixed with 2% aqueous osmium tetroxide, and 3 more rinses with Millipore water. A graded series of ethanol concentrations from 30-100% was incorporated as the initial dehydrant followed by propylene oxide as a final dehydrant. Samples were gradually infiltrated with 3 increasing propylene oxide and Embed 812 ratios up to full resin under vacuum. Samples were allowed to infiltrate in pure resin overnight on a rotator. The samples were embedded into flat silicone molds and cured in the oven at 62^{o}C for three days. The polymerized samples were sectioned and stained with 1% uranyl acetate for 10 minutes followed by lead citrate for 1 minute before TEM examination. TEM images were captured using a JEOL JEM 1010 transmission electron microscope with an AMT XR-16 mid-mount 16 mega-pixel digital camera.

Statistical analyses

Comparisons between pairs of datasets were made using Student's t-test. Multiple datasets were first compared using One-way ANOVA. Pairwise comparisons were made within the ANOVA test by applying the Bonferroni post-hoc correction.

STATISTICS (related to the data shown in all figures)

All values represent mean ±SEM

Figure 1G Bouton number: WT = 68.2±3, *iav*^{1} = 37.1±1.9; *iav*^{1}/Df1 = 37.6±2, and *iav*^{1}/Df2 = 37.7±3.3; *iav*^{3621} = 41±2.6; *iav*^{1}/*iav*^{3621} = 45.2±2.2; *iav*^{1}; P[*iav*$^{+}$] = 61±2.3 ; *UAS-iav*^{JR} = 58.3±3.9, *ok371-GAL4* = 69.5±4.7, *ok371>iav*^{JR} = 45.2±2.5

Figure 1H Bouton number: WT = 23.9±1.1, *iav*^{1} = 16.1±1, *iav*^{1};P[*iav*$^{+}$] = 21.1±1.1

Figure 1I Volume per bouton (μm^3): WT = 1±0.2, *iav*^{1} = 2.3±0.5, *iav*^{1}; P[*iav*$^{+}$] = 0.6±0.2

Figure 1J Bouton number: *iav*^{1}; *UAS-iav* = 39.5±3.0, *iav*^{1}; *ok371-GAL4* = 44.3±2.9, *iav*^{1}; *ok371>iav* = 58.1±2.5, *iav*^{1};;*d42-GAL4* = 40.8±3.3, *iav*^{1}; *d42>iav* = 64.9±4.1, *iav*^{1}; *ato-GAL4* = 37.8±3.4, *iav*^{1}; *ato>iav* = 42.5±3.2, *iav*^{1}, *mef2>iav* = 34.8±2.5

Figure 2J Bouton number: *iav*^{1}; *UAS-TRPV1* = 43.3±2.5, *iav*^{1}; *ok371>hTRPV1* = 67.7±3.2, *ok371>hTRPV1* = 67.2±6; *iav*^{1}; *ok371>hTRPV4* = 41.3±1.9; *iav*^{1}; *ok371>nan* = 40.9±2.8

Figure 2K Bouton number in *iav*^{1}*; ok371>hTRPV1*: 0 μM CPZ = 83.9±3.6, 100 μM CPZ = 74.4±2.2, 300 μM CPZ = 52.2±2.0

Figure 2L Bouton number in *iav*^{1};P[*iav*$^{+}$]: 0 μM CPZ = 64.3±3.2, 300 μM CPZ = 71.5±4.7

Figure 2M Bouton number: *UAS-NaChBac* = 65.9±4.2, iav^{1}; *UAS-NaChBac* = 40.9±3.7, *ok371>NaChBac* = 69.0±2.2, iav^{1}; *ok371>NaChBac* = 53.1±2.3

Figure 3E Number of Futsch loops per NMJ: iav^{1}; P[iav^{+}] = 5.9±0.4, iav^{1} = 2.9±0.5

Figure 4O Bouton numbers: *UAS-canA1*^{IR} = 72.6±5.1, *ok371>canA1*^{IR} = 47.7±2.2, iav^{1}*; ok371>canA1*^{IR} = 47.9±1.9

Figure 4P Bouton numbers: iav^{1}; *UAS-canA1*^{CA} = 42.9±1.6, iav^{1}; *ok371>canA1*^{CA} = 60.2±2.5, *UAS-canA1*^{CA} = 59.2±2.6, *ok371>canA1*^{CA} = 54.2±1.6

Figure 4Q Number of Futsch loops per NMJ: iav^{1}; *UAS-canA1*^{CA} = 3.6±0.4, iav^{1}; *ok371>canA1*^{CA} = 7.4±0.5, *UAS-canA1*^{CA} = 7.0±0.5, *ok371>canA1*^{CA} = 6.2±0.6

Figure 4R Bouton numbers: iav^{1}; *UAS-sgg*^{DN} = 42.1±1.9, iav^{1}*; ok371>sgg*^{DN} = 65.6±3.8, *UAS-sgg*^{DN} = 68.4±3.6, *ok371>sgg*^{DN} = 75.6±3.5

Figure 5J Bouton numbers: *UAS-serca*^{IR} = 66.1±1.9, *ok371>serca*^{IR} = 49.0±2.4, iav^{1}; *ok371>serca*^{IR} = 41.6±2.7, *Kum*^{170}/+ = 46.1±5.7; *RyR*^{16}/+ = 47.3±2.8, iav^{1}; *RyR*^{16}/+ = 41.4±1.9, *UAS-itpr*^{IR} = 66.8±2.7; *elav>itpr*^{IR} = 43.5±3.0, *ok371>itpr*^{IR} = 40.9±2.7, iav^{1}; *UAS-itpr*^{IR} = 41.6±2.9, iav^{1}; *ok371>itpr*^{IR} = 41.9±3.0

Figure 5K Relative bouton area, *UAS-serca*^{IR} = 1±0.06, *ok371>serca*^{IR} = 1.7±0.1, +/+ = 1±0.03, *RyR*^{16}/+ = 1.6±0.05

Figure 5L Bouton numbers: iav^{1} = 37.1±1.9, iav^{1}; *RyR*^{24D03}/+ = 52.1±1.8, *RyR*^{24D03}/+ = 46.5±2.1

Figure 5M Relative ER Ca^{2+} levels: Iav control = 0.97±0.06, Iav overexpressing = 0.49±0.04; TRPV1 control = 1±0.07, TRPV1 overexpressing = 0.46±0.05; TRPV4 control = 1±0.02, TRPV4 overexpressing = 0.88±0.06

Figure 7C Intensity Ratios (GCAMP5G;tdTomoato): At $[Ca^{2+}]_{ext}$ = 1.5 mM, WT = 0.102±0.014, *iav*^{1} = 0.112±0.026; $[Ca^{2+}]$ = 0.5 mM, WT = 0.112±0.012, *iav*^{1} = 0.070±0.015; $[Ca^{2+}]$ = 0 mM, WT = 0.101±0.013, *iav*^{1} = 0.059±0.009

Figure 7E EJP amplitudes: *iav*^{1}; [*iav*$^{+}$]= 25.8±2.7, *iav*^{1} = 12.4±1.1, *iav*^{1}/Df = 12.7±1.9, *iav*^{1}; *ok371>iav* = 25.5±2.5, *canA1*$^{-/+}$ = 24.1±4.6, *canA1*$^{-/Df\text{-}canA1}$ = 22.3±3.1

Figure 7F Quantal content: *iav*^{1}; P[*iav*$^{+}$] = 18.8±2.1, *iav*^{1} = 8.6±1.2, *iav*^{1}/Df1 = 8.8±1.1, *iav*^{1}; *ok371>iav* = 20.5±2.5

Figure 7G Relative quantal content: At $[Ca^{2+}]_{ext}$ = 0.25 mM, *iav*^{1}; P[*iav*$^{+}$] = 1±0.1, *iav*^{1} = 0.3±0.1; $[Ca^{2+}]$ = 0.4 mM, *iav*^{1}; P[*iav*$^{+}$] = 1±0.1, *iav*^{1} = 0.6±0.1; $[Ca^{2+}]$ = 0.75 mM, *iav*^{1}; P[*iav*$^{+}$] = 1±0.1, *iav*^{1} = 0.9±0.2

Figure 7I Paired-pulse ratio normalized to the genomic rescue mean (%): *iav*^{1}; P[*iav*$^{+}$] = 95.0±7.8, *iav*^{1} = 134.7±10.5, *iav*^{1}/Df1 = 142.9±12.5, *iav*^{1}; *ok371>iav* = 112.8±3.2

Figure 7J EJP amplitudes: *iav*^{1}; P[*iav*$^{+}$] = 25.8±2.7, *ok371>iav* = 40±3.6

Figure 7K Quantal content: *iav*^{1}; P[*iav*$^{+}$] = 18.8±1.9, *ok371>iav* = 30.9±2.0

Figure 7L Paired-pulse ratio normalized to the genomic rescue mean (%): *iav*^{1}; *ok371>iav* = 112.8±3.2, *ok371>iav* = 79.9±4.0

Figure S2G Bouton numbers: $canA1^{-/+}$ = 67.9±4.9, $canA1^{-/Df\text{-}canA1}$ = 45.2±3.4, *UAS-*$canA1^{FB5}$ = 82.6±2.9, *ok371>UAS-*$canA1^{FB5}$ = 53.3±2.7

Figure S2H Relative bouton areas: *UAS-*$canA1^{IR}$ = 1±0.05, *ok371>*$canA1^{IR}$ = 1.8±0.1, $canA1^{-/+}$ = 1±0.07, $canA1^{-/Df\text{-}canA1}$ = 2.0±0.3, iav^{1}*; ok371>*$canA1^{CA}$ = 1±0.1, iav^{1}; *UAS-*$canA1^{CA}$ = 1.5±0.1

Figure S2I Bouton numbers: WT = 68.2±3.0, $futsch^{N94}$ = 49.4±1.8, $futsch^{N94}$; *UAS-*$canA1^{CA}$ = 49.8±1.4; $futsch^{N94}$; *d42>*$canA1^{CA}$ = 47.9±2.1

Figure S4A mEJP amplitudes: iav^{1}; P[iav^{+}] = 1.4±0.1, iav^{1} = 1.6±0.2, iav^{1}/Df1 = 1.4±0.1, iav^{1}; *ok371>iav* = 1.3±0.1, *ok371>iav* = 1.4±0.2, $canA1^{-/+}$ = 1.6±0.1, $canA1^{-/Df\text{-}canA1}$ = 1.55±0.05

Figure S4B mEJP frequencies: iav^{1}; P[iav^{+}] = 1.9±0.3, iav^{1} = 2.4±0.3, iav^{1}/Df1 = 2.2±0.3, iav^{1}; *ok371>iav* = 1.7±0.2, *ok371>iav* = 2.2±0.5

Figures S4C Quantal content: At $[Ca^{2+}]_{ext}$ = 0.25 mM, iav^{1}; P[iav^{+}] = 1.9±0. 2, iav^{1} = 0.6±0.1; $[Ca^{2+}]$ = 0.4 mM, iav^{1}; P[iav^{+}] = 10.6±0.7, iav^{1} = 5.9±0.5; $[Ca^{2+}]$ = 0.5 mM, iav^{1}; P[iav^{+}] = 18.8±1.9, iav^{1} = 8.6±1.1; $[Ca^{2+}]$ = 0.75 mM, iav^{1}; P[iav^{+}] = 26.9±2.5, iav^{1} = 24.3±3.8

Figure S5D SV number/bouton area: iav^{1}; P[iav^{+}] = 8.5±2.8, iav^{1} = 8.8±1.2

Figure S5E SV number/AZ length: iav^{1}; P[iav^{+}] = 9.3±1.1, iav^{1} = 9.5±1.9

Figure S5F SV diameter: iav^{1}; P[iav^{+}] = 38.9±0.7, iav^{1} = 38.9±0.9

Figure S5G Quantal content values from Figure S4C plotted in $\log_{10}$ scale.

Figure S5H Bouton numbers: *UAS-iav* = 67.3±3.8, *ok371>iav* = 44.8±2.0, *d42>iav* = 44.7±2.1

Figure S5I Number of Brp punctae per NMJ: *UAS-iav* = 474.4±21.9, *ok371>iav* = 513.6±33.0

SUPPLEMENTAL TABLE 1 (Related to Figure 1)

NMJ bouton counts in TRP mutants at larval A3 segment, muscles 6/7.

	Genotype	Bouton Count (mean ± S.E.M)
	WT (Canton-S)	68.2±3.0
TRPC	*trp*^{1}	68±3.2
	trpγ^{G4}	67.4±3.9
	trpL^{302}	71.4±4.8
TRPA	*pain*^{GAL4}	64.4±3.2
	pyx^{3}	71.8±5.0
	trpA1^{1}	68.4±4.5
	wtrw^{2}	63.9±4.5
TRPV	*nan*^{36a}/*Df*^{nan}	73.8±5.7
	iav^{1}	37.1±1.9

SUPPLEMENTAL REFERENCES

Bourouis, M. (2002). Targeted increase in shaggy activity levels blocks wingless signaling. Genesis *34*, 99-102.

Brand, A.H., and Perrimon, N. (1993). Targeted gene expression as a means of altering cell fates and generating dominant phenotypes. Development *118*, 401-415.

Dijkers, P.F., and O'Farrell, P.H. (2007). Drosophila calcineurin promotes induction of innate immune responses. Curr Biol *17*, 2087-2093.

Feeney, C.J., Karunanithi, S., Pearce, J., Govind, C.K., and Atwood, H.L. (1998). Motor nerve terminals on abdominal muscles in larval flesh flies, Sarcophaga bullata: comparisons with Drosophila. J Comp Neurol *402*, 197-209.

Gao, S., Sandstrom, D.J., Smith, H.E., High, B., Marsh, J.W., and Nash, H.A. (2013). Drosophila ryanodine receptors mediate general anesthesia by halothane. Anesthesiology *118*, 587-601.

Gong, Z., Son, W., Chung, Y.D., Kim, J., Shin, D.W., McClung, C.A., Lee, Y., Lee, H.W., Chang, D.J., Kaang, B.K., *et al.* (2004). Two interdependent TRPV channel subunits, inactive and Nanchung, mediate hearing in *Drosophila*. J Neurosci *24*, 9059-9066.

Hassan, B.A., Bermingham, N.A., He, Y., Sun, Y., Jan, Y.N., Zoghbi, H.Y., and Bellen, H.J. (2000). atonal regulates neurite arborization but does not act as a proneural gene in the Drosophila brain. Neuron *25*, 549-561.

Jan, L.Y., and Jan, Y.N. (1976). Properties of the larval neuromuscular junction in Drosophila melanogaster. J Physiol *262*, 189-214.

Kim, J., Chung, Y.D., Park, D.Y., Choi, S., Shin, D.W., Soh, H., Lee, H.W., Son, W., Yim, J., Park, C.S.*, et al.* (2003). A TRPV family ion channel required for hearing in *Drosophila*. Nature *424*, 81-84.

Kwon, Y., Shen, W.L., Shim, H.S., and Montell, C. (2010). Fine thermotactic discrimination between the optimal and slightly cooler temperatures via a TRPV channel in chordotonal neurons. J Neurosci *30*, 10465-10471.

Kwon, Y., Shim, H.S., Wang, X., and Montell, C. (2008). Control of thermotactic behavior via coupling of a TRP channel to a phospholipase C signaling cascade. Nat Neurosci *11*, 871-873.

Lee, Y., Lee, Y., Lee, J., Bang, S., Hyun, S., Kang, J., Hong, S.T., Bae, E., Kaang, B.K., and Kim, J. (2005). Pyrexia is a new thermal transient receptor potential channel endowing tolerance to high temperatures in Drosophila melanogaster. Nat Genet *37*, 305-310.

Littleton, J.T., Stern, M., Perin, M., and Bellen, H.J. (1994). Calcium dependence of neurotransmitter release and rate of spontaneous vesicle fusions are altered in Drosophila synaptotagmin mutants. Proc Natl Acad Sci U S A *91*, 10888-10892.

Luan, H., Lemon, W.C., Peabody, N.C., Pohl, J.B., Zelensky, P.K., Wang, D., Nitabach, M.N., Holmes, T.C., and White, B.H. (2006). Functional dissection of a neuronal network required for cuticle tanning and wing expansion in Drosophila. J Neurosci *26*, 573-584.

Marella, S., Fischler, W., Kong, P., Asgarian, S., Rueckert, E., and Scott, K. (2006). Imaging taste responses in the fly brain reveals a functional map of taste category and behavior. Neuron *49*, 285-295.

Meyer, F., and Aberle, H. (2006). At the next stop sign turn right: the metalloprotease Tolloid-related 1 controls defasciculation of motor axons in Drosophila. Development *133*, 4035-4044.

Montell, C., Jones, K., Hafen, E., and Rubin, G. (1985). Rescue of the Drosophila phototransduction mutation trp by germline transformation. Science *230*, 1040-1043.

Nakai, Y., Horiuchi, J., Tsuda, M., Takeo, S., Akahori, S., Matsuo, T., Kume, K., and Aigaki, T. (2011). Calcineurin and its regulator sra/DSCR1 are essential for sleep in Drosophila. J Neurosci *31*, 12759-12766.

Niemeyer, B.A., Suzuki, E., Scott, K., Jalink, K., and Zuker, C.S. (1996). The Drosophila light-activated conductance is composed of the two channels TRP and TRPL. Cell *85*, 651-659.

Pauli, A., Althoff, F., Oliveira, R.A., Heidmann, S., Schuldiner, O., Lehner, C.F., Dickson, B.J., and Nasmyth, K. (2008). Cell-type-specific TEV protease cleavage reveals cohesin functions in Drosophila neurons. Dev Cell *14*, 239-251.

Ranganayakulu, G., Schulz, R.A., and Olson, E.N. (1996). Wingless signaling induces nautilus expression in the ventral mesoderm of the Drosophila embryo. Dev Biol *176*, 143-148.

Roos, J., Hummel, T., Ng, N., Klambt, C., and Davis, G.W. (2000). Drosophila Futsch regulates synaptic microtubule organization and is necessary for synaptic growth. Neuron *26*, 371-382.

Sanyal, S., Consoulas, C., Kuromi, H., Basole, A., Mukai, L., Kidokoro, Y., Krishnan, K.S., and Ramaswami, M. (2005). Analysis of conditional paralytic mutants in

Drosophila sarco-endoplasmic reticulum calcium ATPase reveals novel mechanisms for regulating membrane excitability. Genetics *169*, 737-750.

Snapp, E.L., Iida, T., Frescas, D., Lippincott-Schwartz, J., and Lilly, M.A. (2004). The fusome mediates intercellular endoplasmic reticulum connectivity in Drosophila ovarian cysts. Mol Biol Cell *15*, 4512-4521.

Sullivan, K.M., Scott, K., Zuker, C.S., and Rubin, G.M. (2000). The ryanodine receptor is essential for larval development in Drosophila melanogaster. Proc Natl Acad Sci U S A *97*, 5942-5947.

Sweeney, S.T., and Davis, G.W. (2002). Unrestricted synaptic growth in *spinster*-a late endosomal protein implicated in TGF-β-mediated synaptic growth regulation. Neuron *36*, 403-416.

Tracey, W.D., Jr., Wilson, R.I., Laurent, G., and Benzer, S. (2003). painless, a Drosophila gene essential for nociception. Cell *113*, 261-273.

Yao, C.K., Lin, Y.Q., Ly, C.V., Ohyama, T., Haueter, C.M., Moiseenkova-Bell, V.Y., Wensel, T.G., and Bellen, H.J. (2009). A synaptic vesicle-associated Ca2+ channel promotes endocytosis and couples exocytosis to endocytosis. Cell *138*, 947-960.

Figure S1 (related to Figure 2)

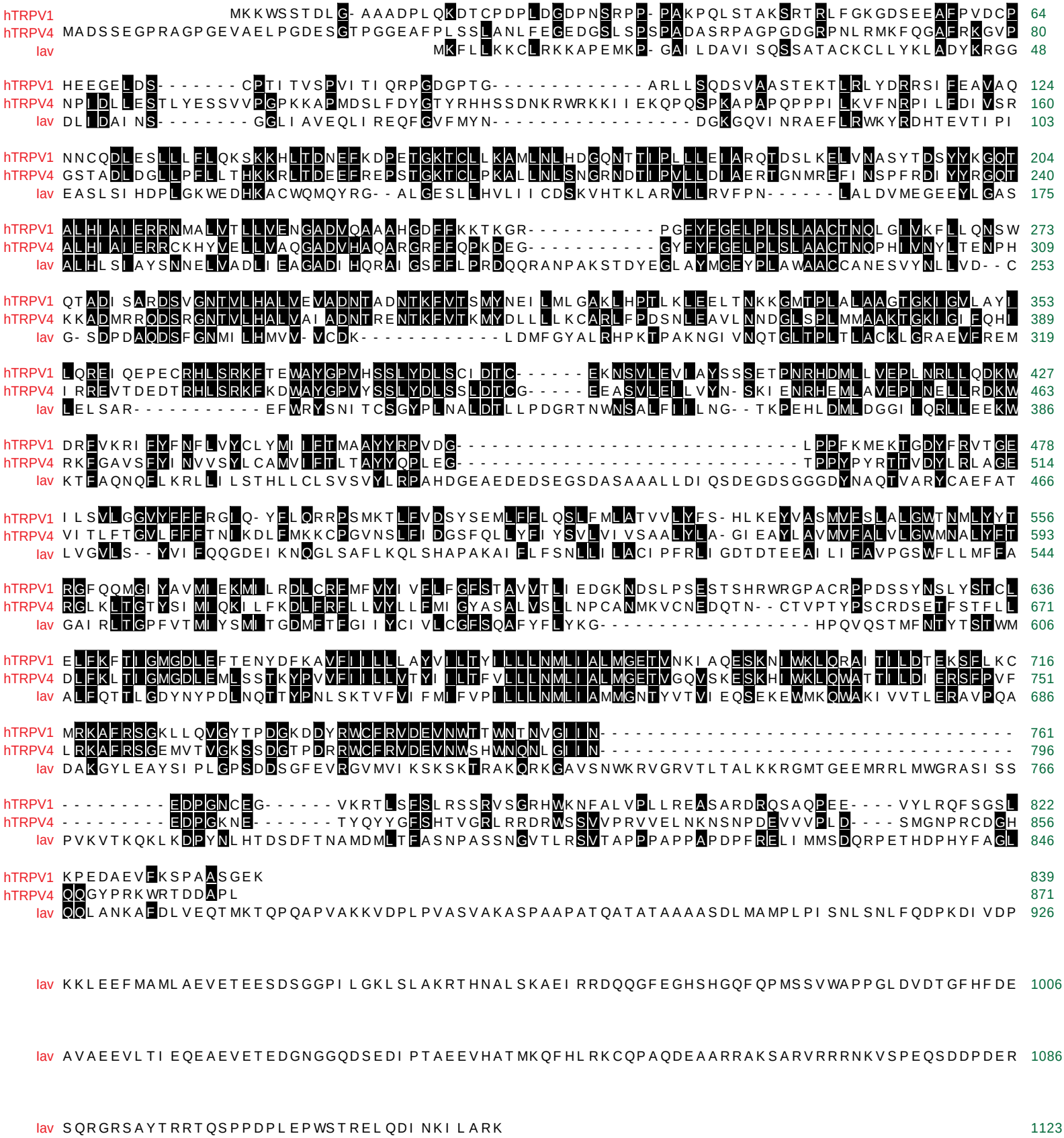

FIGURE S1. Alignment of the primary amino acid sequences of human TRPV1, human TRPV4, and *Drosophila* Iav. The numerical values on the right indicate the positions of the amino acids in the 3 proteins. Black shaded boxes indicate residues that are conserved in at least 2 of the 3 proteins being aligned.

Figure S2 (related to Figure 4)

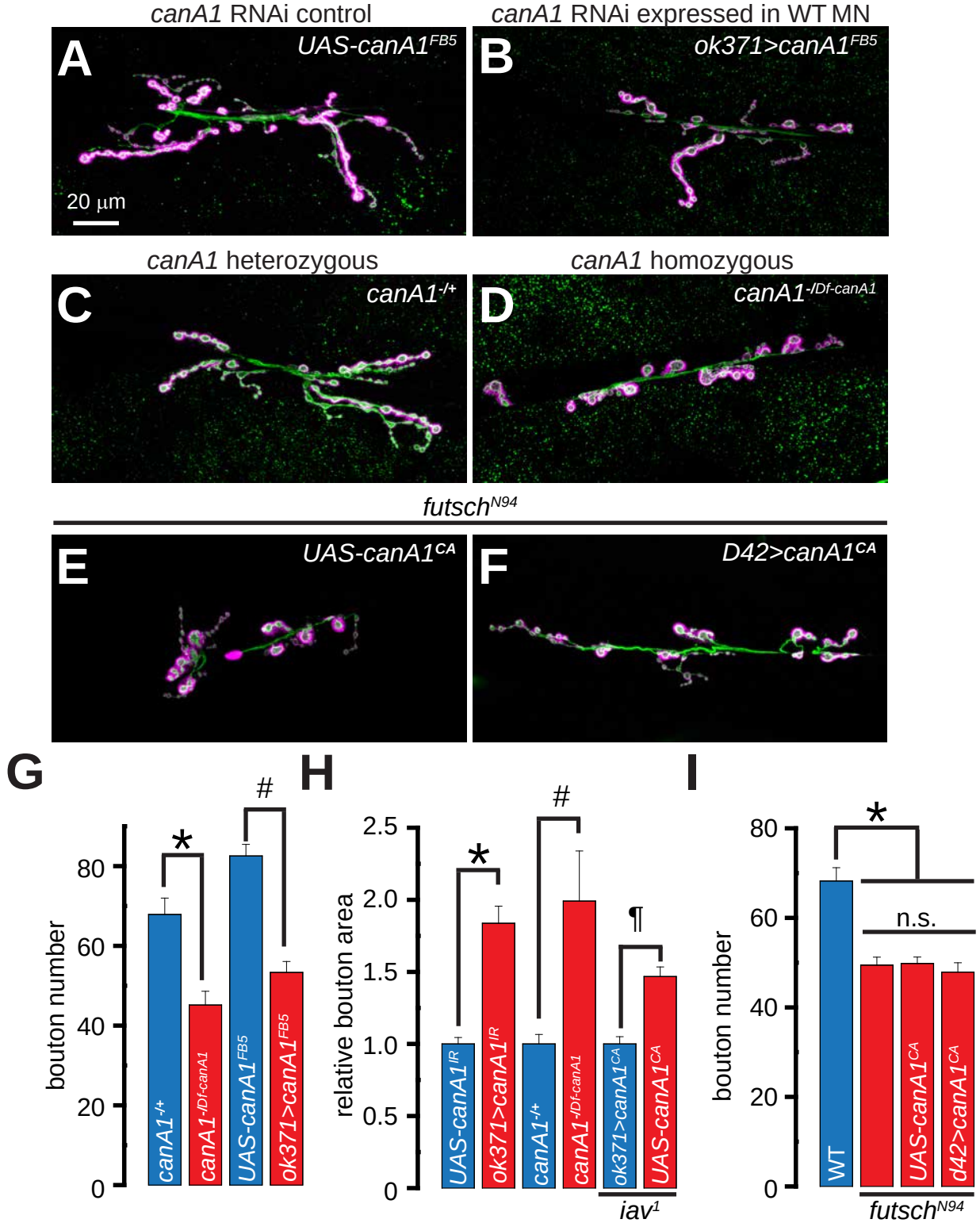

FIGURE S2. Calcineurin regulates NMJ bouton numbers and morphology via Futsch

(A-F) Representative confocal image of 3rd instar larval NMJs from larvae of the indicated genotypes stained with antibodies against the presynaptic marker, HRP (green) and the postsynaptic marker, DLG (magenta). Scale bar shown in (A) also applies to (B-F).

(G) Quantification of the NMJ bouton numbers in larvae of the indicated genotypes. *, $p = 5.4 \times 10^{-4}$, #, $p = 4.7 \times 10^{-6}$, unpaired Student's t-tests, n = 7-21 NMJs per genotype.

(H) Quantification of the relative bouton area in larvae of the indicated genotypes. *, $p = 1.7 \times 10^{-4}$; #, $p = 0.02$; ¶ = 3.4×10^{-5}; unpaired Student's t-tests, n =7-16 NMJs per genotype.

(I) Quantification of the NMJ bouton numbers in larvae of the indicated genotypes. *, $p = 9.3 \times 10^{-9}$, one-way ANOVA (comparing all the data sets), n = 16-30 NMJs per genotype.

All values represent mean ±SEM. Please consult the *Supplementary Files* for all values.

Abbreviations: WT, wild-type; MN, motor neuron.

Figure S3 (related to Figure 6)

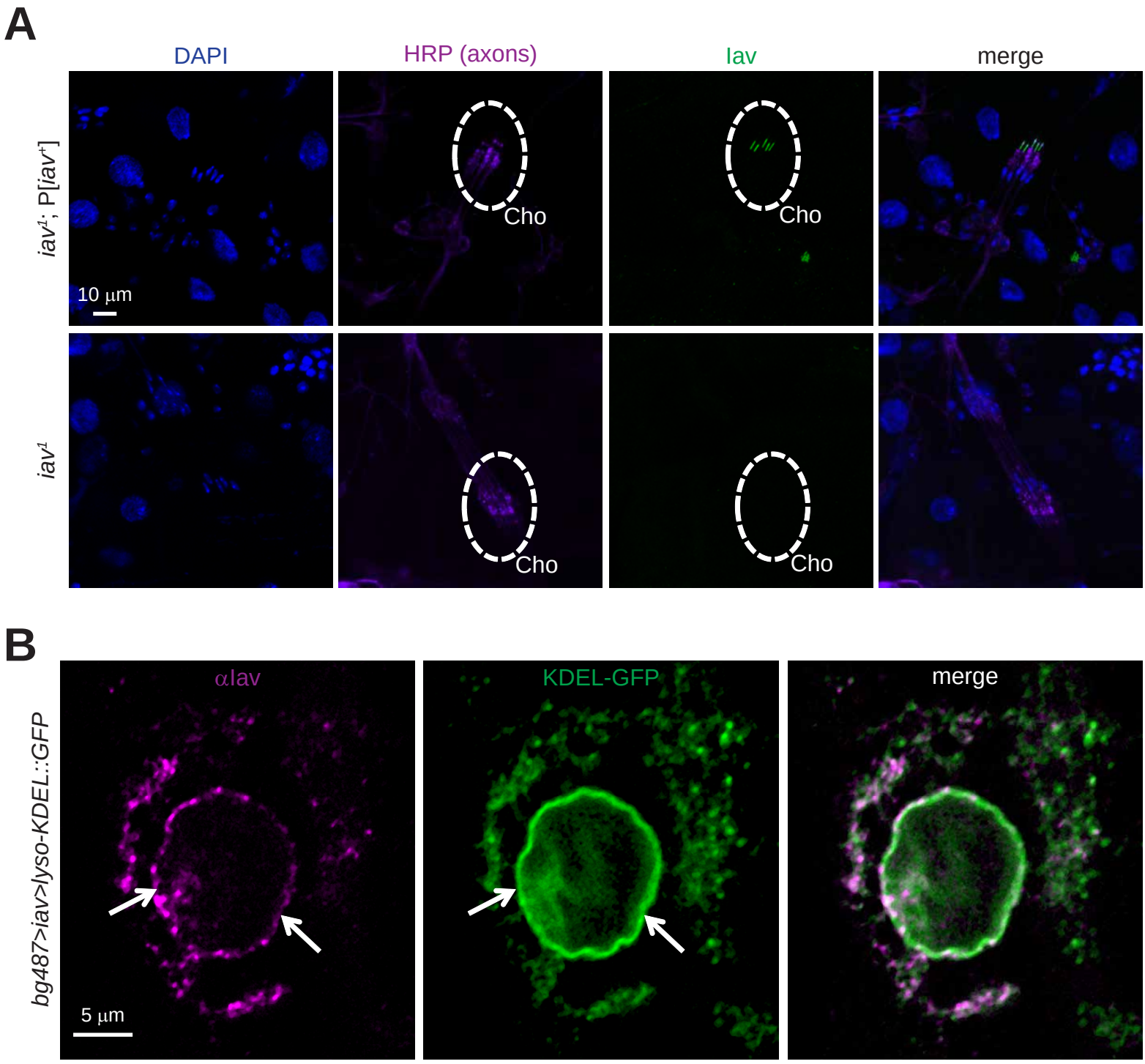

FIGURE S3. Iav expression in larval chordotonal neurons and muscle
(A) Representative confocal images of larval chordotonal neurons in larvae of the indicated genotypes stained with DAPI (blue), the neuronal marker, anti-HRP (purple), anti-Iav (green). *Dashed ovals* indicate chordotonal dendrites exhibiting Iav expression. Scale bar shown in the panel on the top-left applies to all panels.
(B) Representative confocal images of larval muscle of the indicated genotypes stained anti-Iav (magenta) and KDEL-GFP (green). *Arrows* indicate colocalization at the nuclear envelope. Scale bar shown in the panel on the left applies to all panels.

Figure S4 (related to Figure 7)

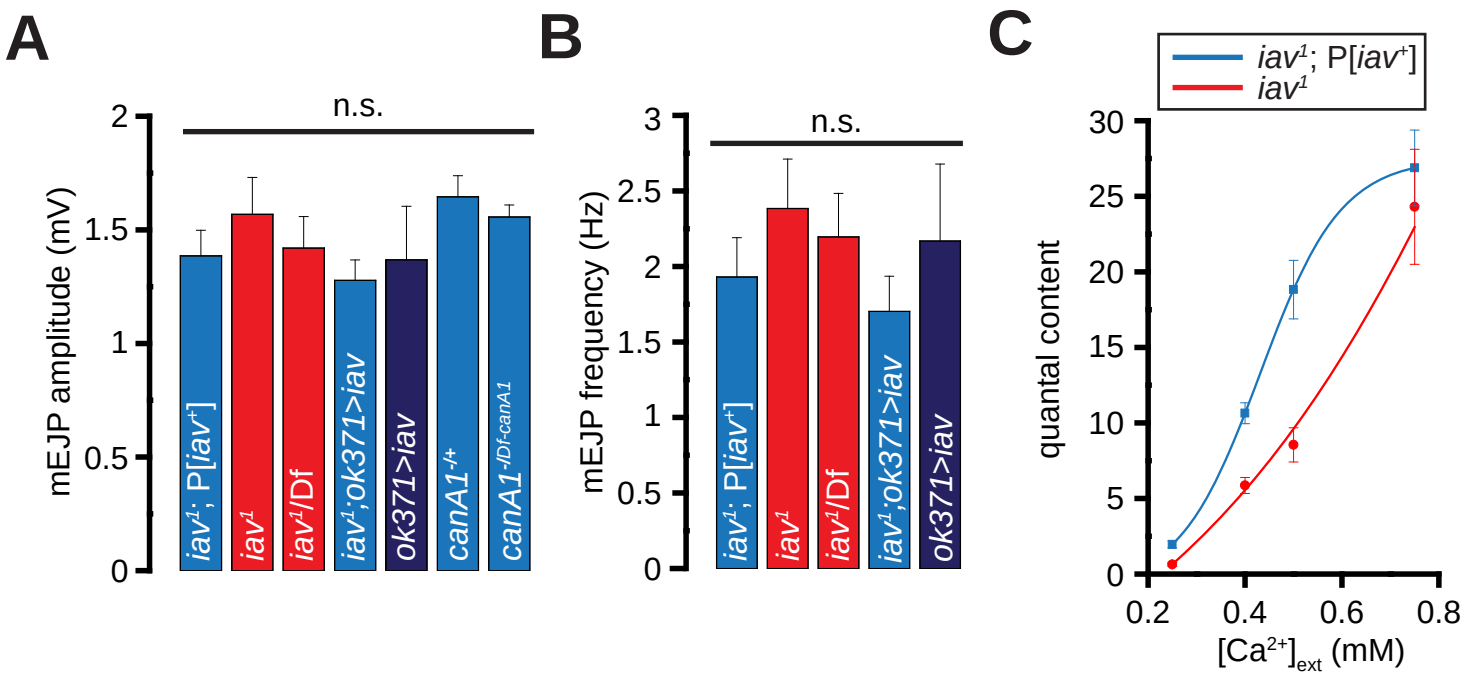

FIGURE S4. Alterations in evoked neurotransmission at the *iav*^{1} NMJs

(A) Quantification of the amplitude of the mEJPs obtained from recordings performed at 0.5 mM Ca^{2+} on larvae of the indicated genotypes.

(B) Quantification of the frequency of the mEJPs obtained from recordings performed at 0.5 mM Ca^{2+} on larvae of the indicated genotypes.

(C) Quantification of the quantal content obtained from recordings performed on larvae of the indicated genotypes at the indicated extracellular Ca^{2+} concentrations ($[Ca^{2+}]_{ext}$). The blue and red curves were obtained by fitting the respective mean values to sigmoidal functions using Origin6 (OriginLab corporation).

All values represent mean ±SEM. Please consult the *Supplementary Files* for all values and information on statistical tests employed. Abbreviations: n.s., not significant.

Figure S5 (related to Figure 7)

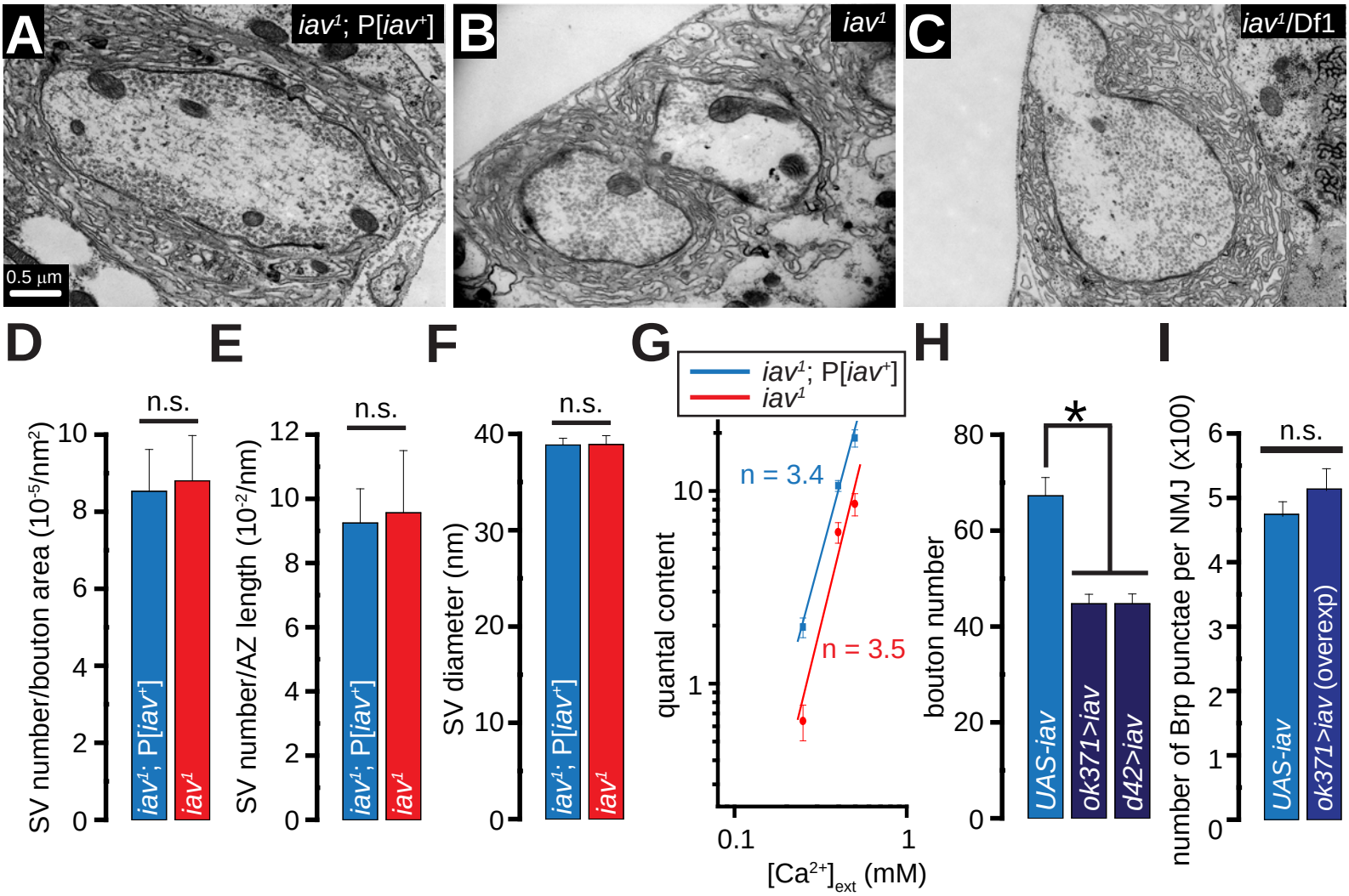

FIGURE S5. The *iav*^{1} synaptic boutons do not exhibit ultrastructural alterations in SV release machinery
(A-C) Transmission electron micrographs of boutons from muscle 6 of 3rd instar larvae of the indicated genotypes. Scale bar shown in (A) apply to (A-C).
(D-F) Quantification of then indicated parameters in the indicated genotypes.
(G) Quantification of the Ca^{2+} cooperativity of SV release in larvae of the indicated genotypes at the indicated extracellular Ca^{2+} concentrations ($[Ca^{2+}]_{ext}$). Both axes are in the $\log_{10}$ scale. The blue and red lines were obtained by linear fitting of the respective mean values using Origin6 (OriginLab corporation). “n” refers to the slope of the lines.
(H) Quantification of the bouton numbers in the indicated genotypes. *, $p = 1.01 \times 10^{-7}$, one-way ANOVA, n = 15-19 NMJs per genotype.
(I) Quantification of the number of Brp punctae per NMJ in larvae of the indicated genotypes.
All values represent mean ±SEM. Please consult the *Supplementary Files* for all values and information on statistical tests employed. Abbreviations: n.s., not significant.